



# Failure Characteristics of Granite Influenced by Sample Height-to-Width Ratios and Intermediate Principal Stress Under True-Triaxial Unloading Conditions

Xibing Li<sup>1</sup> · Fan Feng<sup>1,2</sup> · Diyuan Li<sup>1</sup>  · Kun Du<sup>1</sup> · P. G. Ranjith<sup>3</sup> · Jamal Rostami<sup>2</sup>

Received: 13 June 2017 / Accepted: 19 January 2018 / Published online: 1 February 2018  
© Springer-Verlag GmbH Austria, part of Springer Nature 2018

## Abstract

The failure modes and peak unloading strength of a typical hard rock, Miluo granite, with particular attention to the sample height-to-width ratio (between 2 and 0.5), and the intermediate principal stress was investigated using a true-triaxial test system. The experimental results indicate that both sample height-to-width ratios and intermediate principal stress have an impact on the failure modes, peak strength and severity of rockburst in hard rock under true-triaxial unloading conditions. For longer rectangular specimens, the transition of failure mode from shear to slabbing requires higher intermediate principal stress. With the decrease in sample height-to-width ratios, slabbing failure is more likely to occur under the condition of lower intermediate principal stress. For same intermediate principal stress, the peak unloading strength monotonically increases with the decrease in sample height-to-width. However, the peak unloading strength as functions of intermediate principal stress for different types of rock samples (with sample height-to-width ratio of 2, 1 and 0.5) all present the pattern of initial increase, followed by a subsequent decrease. The curves fitted to octahedral shear stress as a function of mean effective stress also validate the applicability of the Mogi–Coulomb failure criterion for all considered rock sizes under true-triaxial unloading conditions, and the corresponding cohesion  $C$  and internal friction angle  $\varphi$  are calculated. The severity of strainburst of granite depends on the sample height-to-width ratios and intermediate principal stress. Therefore, different supporting strategies are recommended in deep tunneling projects and mining activities. Moreover, the comparison of test results of different  $\sigma_2/\sigma_3$  also reveals the little influence of minimum principal stress on failure characteristics of granite during the true-triaxial unloading process.

**Keywords** True-triaxial unloading · Sample height-to-width ratios · Intermediate principal stress · Failure modes · Failure criterion · Rockburst

## 1 Introduction

The increasing demand for resources and exhausting of reserves at shallow depths has driven more mining and tunneling projects into higher depth in situ stress conditions. Underground rock masses are subjected to a general stress state with  $\sigma_1 > \sigma_2 > \sigma_3$ , where  $\sigma_1$ ,  $\sigma_2$  and  $\sigma_3$  are the maximum, intermediate and minimum principal stresses, respectively (Mogi 2007; He et al. 2010; Feng et al. 2016). A large amount of energy is stored in deep, highly stressed, hard rocks, and the excavation of underground workings allows for release and transfer of some stored energy in the surrounding rock. This release of energy may lead to a severe failure of the highly stressed rock mass. Field monitoring in many hard rock mines has recorded dynamic failure phenomena such as rockburst, caving, and chamber instability

✉ Fan Feng  
fengfan0213@126.com

✉ Diyuan Li  
diyuan.li@csu.edu.cn

<sup>1</sup> School of Resources and Safety Engineering, Central South University, Changsha, Hunan, People's Republic of China

<sup>2</sup> Department of Mining Engineering, Earth Mechanics Institute, Colorado School of Mines, Golden, CO, USA

<sup>3</sup> Deep Earth Laboratory, Department of Civil Engineering, Monash University, Building 60, Melbourne, VIC, Australia

(Pechmann et al. 1995; Blake and Hedley 2003; Wen et al. 2016). In these incidents, where potential for severe rockburst is high, the hard, brittle rocks may exhibit distinct mechanical behavior compared with those in shallow geological conditions, where surface-parallel slabbing and spalling failure is the dominant and prevailing phenomena near excavation boundaries (Zhu et al. 2014). According to Ortlepp (1997), spalling or slabbing is generally defined as the formation of stress-induced slabs parallel to the walls on the boundary of an underground excavation. Martin and Maybee (2000) observed that the dominant failure mode was progressive slabbing and spalling rather than shear in pillars of some Canadian hard rock mines. Because of neglecting the influence of the intermediate principal stress, the empirical Mohr–Coulomb and Hoek–Brown criteria are therefore inappropriate for modeling above-mentioned failure phenomena and characteristics (Vernik and Zoback 1992; Diederichs 2007; Li et al. 2015).

The influence of intermediate principal stress on rock fracturing has been studied by many researchers in true-triaxial testing and numerical simulations (Mogi 1970, 1971a; Haimson and Chang 2000, 2002; Chang and Haimson 2000; Al-Ajmi and Zimmerman 2005; Alexeev et al. 2008; Cai 2008; You 2009; Besuelle and Hall 2011; Lee and Haimson 2011; Ingraham et al. 2013; Jimenez and Ma 2013; Li et al. 2015; Du et al. 2016; Ma and Haimson 2016). Based on the previous studies, Mogi designed a true-triaxial loading compression test that in particular, paid attention to the effect of intermediate principal stress on strength and failure modes of different rock types. His experiments demonstrated that, for the rocks tested, strength is a function of  $\sigma_2$  in a manner similar to that predicted theoretically by Wiebols and Cook (1968). Li et al. (2015) indicated that both the strength and failure modes of cubic rock specimens under true-triaxial unloading conditions are affected by the intermediate principal stress. When  $\sigma_2$  increases to a certain value for strong, hard rocks, the rock failure mode may change from shear to slabbing. Haimson and Chang (2000) designed and fabricated a new true-triaxial cell to conduct an extensive series of tests in Westerly granite. A new true-triaxial strength criterion for the rock was introduced, which accounts for the effect of the intermediate principal stress.

The numerical analysis was also an efficient method to study the progressive failure of rock and rock-like materials. Cai (2008) used combined FEM/DEM (finite element method/discrete element method) modeling and showed that forming of tunnel surface-parallel fractures and microcracks was attributed to material heterogeneity and the existence of relatively high intermediate principal stress, as well as near zero minimum principal stress. Lin et al. (2013) used FLAC 3D to simulate the mechanical properties of layered rock masses under conventional triaxial and true-triaxial compression. Manouchehrian and Cai (2015) adopted

an explicit FEM tool (ABAQUS) to simulate rock failure under polyaxial unloading conditions. Duan et al. (2017) adopted DEM simulations (PFC 2D) to examine the effect of intermediate principal stress on the variations of peak stress, Young's modulus, failure plane angles, brittle–ductile transition, and evolution of failure modes. They found the intermediate principal stress plays an important role on the macroscopic responses and the variation of peak stress as the function of intermediate principal stress exhibits an ascending-then-descending trend.

It should be noted that while much effort has been made to understand strength and failure modes in high-stress conditions, little attention has been paid to the effects of sample size (especially height-to-width ratio) under the conditions of true-triaxial experiments. Figure 1 presents a deep mining roadway in Muluping phosphate mine, Guizhou province, China, where the tunnel section is trapezoidal rather than rectangular or circular. A good understanding of the wall fracture on both sides is necessary for determination of the damage zone, so that roadway support design can be optimized when continuous miners are used to excavate the ore (Li et al. 2013). One of the questions that need to be answered is if rock strength on both sides are similar, or if

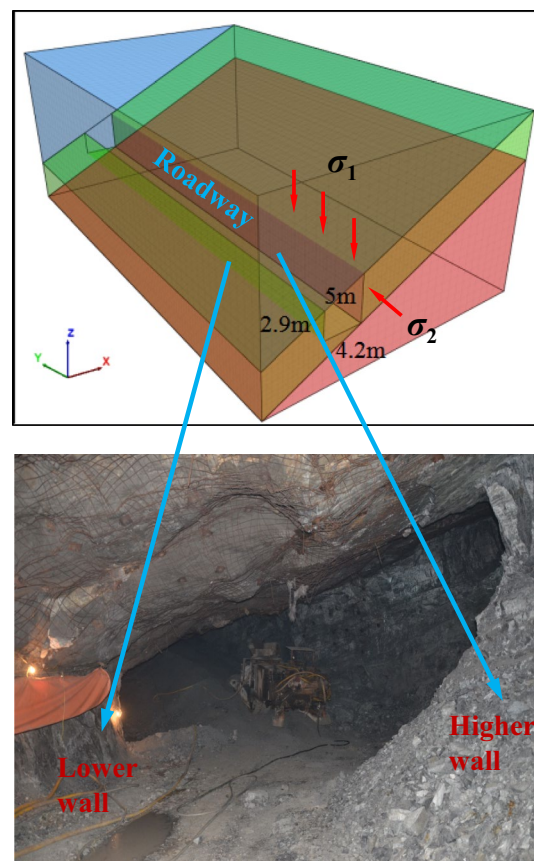


**Fig. 1** Trapezoid-shaped roadway in Muluping phosphate mine, China, at a depth of approximately 900 m

there are conditions that lead to variation in the strength? Also, do the failure characteristics near the excavation (unloading) boundaries represent the combined response of intermediate principal stress and roadway height?

A number of researchers have investigated the effect of height-to-width ratio on uniaxial compressive strength for rocks and for concrete (Gonnerman 1925; Johnson 1943; Obert et al. 1946; Dreyer and Borchert 1961; Mogi 1966; Hudson et al. 1972; Xie et al. 2005; Li et al. 2011). In the 1960s, Mogi (1966) made careful measurements of the apparent compressive strength and fracture angles of Dunham dolomite, Westerly granite, and Mizuho trachyte as functions of the length/diameter ratio ( $L/D$ ). He found that strength decreased markedly with the increase in  $L/D$ , but the value became nearly constant at high values of  $L/D$ . The angle between the fracture and the loading axis also decreased markedly with increase in  $L/D$ . Bazant and Xiang (1997) proposed a fracture mechanics based model to study the influence of effect of specimen size on the strength and failure mode of quasi-brittle materials from the energetic viewpoint. Li et al. (2011) observed that the macrofailure mode will be transformed from shear to slabbing under uniaxial compression when the height-to-width ratio of the prism specimens was reduced to 0.5. Unfortunately, the above-mentioned experiments all examined uniaxial compression, which may not truly reveal the excavation unloading process in deep underground application. Zhao and Cai (2014) presented the results of an experimental study on strainburst behaviors of Tianhu granite with four specimen height-to-width ( $H/W$ ) ratios under the condition of true-triaxial unloading. Similar tests could also be found in Zhao and He (2017). These two experiments found that the failure modes transformed from shear to slabbing failure with the increase in sample height-to-thickness (or height-to-width), and the rock failure strength had an increasing trend with the decreasing  $H/T$  ( $H/W$ ). Note that none of these true-triaxial loading or unloading tests examined the case when sample  $H/W$  was less than 1. This might be due to the difficulties in designing a true-triaxial apparatus that could meet the requirements of these sample sizes.

In the present study, the true-triaxial loading apparatus was designed and successfully tested in the Advanced Research Center, Central South University, to investigate the failure characteristics of typical hard rocks under true-triaxial unloading conditions, with particular attention paid to the different intermediate principal stresses and sample height-to-width ratios. Three groups of rock specimens were prepared, in which the sample height-to-width ratios were 2, 1 and 0.5, respectively. Different loading paths ( $\sigma_2/\sigma_3$ ) were also considered to explore the influence of unloading stress ( $\sigma_3$ ). An acoustic emission monitoring system and a high-speed camera were also adopted to capture the entire failure process. This paper

examines the failure mechanisms of hard rocks, which are influenced by the associated response of intermediate principal stress and sample height-to-width ratios under true-triaxial unloading conditions similar to excavation of different roadway specifications and stress state in deep mining or tunneling projects.

## 2 Experimental Procedures

### 2.1 Specimen Preparation

Rock samples tested were Miluo granite which is typical hard and brittle rock found in Miluo area, Hunan province. Five groups of specimens were prepared from an integrated rock block to maximize the homogeneity among rock samples. They include:

*Group A:* 4 cylindrical specimens, 50 mm in diameter and 100 mm in length;

*Group B:* 4 Brazilian disk specimens, 50 mm in diameter and 25 mm in thickness;

*Group C:* 38 prism specimens, 100 mm × 50 mm × 50 mm, with a sample  $H/W$  of 2.0;

*Group D:* 38 prism specimens, 50 mm × 50 mm × 50 mm, with a sample  $H/W$  of 1.0;

*Group E:* 38 prism specimens, 25 mm × 50 mm × 50 mm, with a sample  $H/W$  of 0.5.

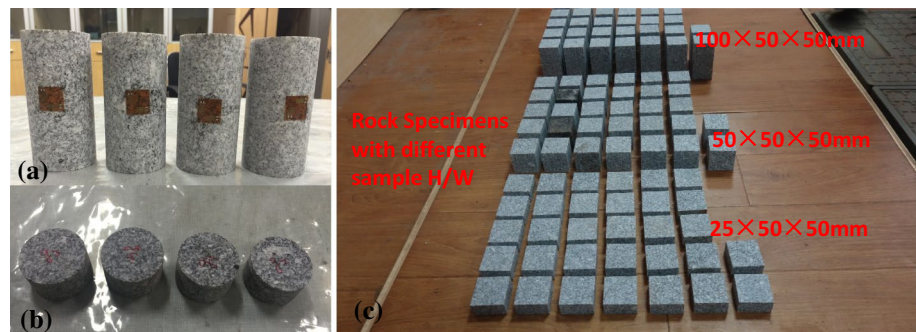
Groups A and B were used to determine the standard uniaxial compressive strength (UCS) and Brazilian indirect tensile strength (BTS) of the rock. Axial and lateral strain gauges were mounted on the specimens. Uniaxial compressive tests of cylindrical specimens were carried out by using a servo-controlled hydraulic testing machine (Model 1346; Instron) and Brazilian tests tested by an Instron 1342 according to the International Society for Rock Mechanics (ISRM) standards. The basic physical and mechanical parameters of Miluo cylindrical granite are listed in Table 1. According to the results of UCS and BTS tests, the Miluo granite can be considered as typical hard rock. Groups C, D and E were used to investigate the influence of the sample  $H/W$  on fracture characteristics of hard rocks under true-triaxial loading conditions. A picture of rock specimen groups is shown in Fig. 2. To minimize the end effects during experiments, all six surfaces of the specimens were polished carefully using a grinding machine to produce smooth end surfaces and good perpendicularity of the specimens. Moreover, the sample  $H/W$  was prepared under strict tolerances to meet the experimental requirements for the evenness and squareness of specimen surfaces to be within 0.02 mm.

**Table 1** The basic physical and mechanical parameters of Miluo cylindrical granite

Average dimension of Group A (mm × mm)	Average dimension of Group B (mm × mm)	Density (g/cm <sup>3</sup> )	Young's modulus (GPa)	Poisson's ratio	Tensile strength (MPa)	UCS (MPa)	Failure mode in uniaxial compression
49.6 × 101.5	50.2 × 25.6	2.49	49.5	0.21	11.2	107.4	Shear

UCS uniaxial compressive strength

**Fig. 2** Overview of five groups of rock specimens showing different sample height-to-width ratios: **a** uniaxial compressive tests; **b** Brazilian tests; **c** true-triaxial unloading tests



## 2.2 True-Triaxial Test System with a Loading Apparatus

The test machine (Model TRW-3000) used in this study is a true-triaxial servo-controlled hydraulic press used for rock testing, as illustrated in Fig. 3. The unit was developed at Central South University, China. This test system can apply quasi-static loading along the three principal stress directions independently through hydraulically driven pistons, with a maximum load of 3000, 2000 and 2000 kN along the vertical ( $Z$ ) and horizontal ( $X$  and  $Y$ ), respectively. This true-triaxial test system has been previously described by Li et al. (2015) and Du et al. (2016). Note that a cubic specimen (usually with the dimension of 100 mm × 100 mm × 100 mm or 200 mm × 200 mm × 200 mm or 300 mm × 300 mm × 300 mm) should be placed in triaxial cell rather than a rectangular prism specimen, which is different from other triaxial test machines (Mogi 1971a; Michelis 1985; Takahashi and Koide 1989; Chen and Feng 2006; He et al. 2007, 2010; Lee and Haimson 2011; Gong et al. 2012; Sriapai et al. 2013; Zhao et al. 2014; Feng et al. 2016). However, three rock dimensions including both cubic and rectangular prism specimens are adopted in the present study. To accommodate the requirement of all sample dimensions, a loading apparatus was designed to accompany the true-triaxial test system (TRW-3000). The testing system in the present study consisted of the main machine, servo-controller, operation control system and the acoustic emission (AE) monitoring system (model PCI-2; Physical Acoustics), as can be seen in Fig. 3a. Six AE transducers are

used to investigate the failure characteristics during the test. Each probe was attached to the corresponding platen. The AE trigger level was set to 40 dB, and the data acquisition rate was set to 0.5 MHz. A high-speed camera (FASTCAM SA1.1) was utilized to observe the abrupt and violent fracturing processes during the test and at the point of failure. Images of the testing apparatus while in use with different sample  $H/W$  are shown in Fig. 3b–d.

The loading machine consisted of a box made up of hard resin, six platens (four in horizontal direction and two in vertical direction) made of manganese steel and several heel blocks made of manganese steel if necessary (used only for sample  $H/W$  is 0.5). Four grooves in each side of box were reserved to place the horizontal platens. Note that a 2 mm gap was left between the groove size and platen to avoid extrusion and distortion of the box during the loading process. Note that the gap should not be too large since the loading direction may deviate to some extent. The platen material has extremely high stiffness and rigidity that can bear and transfer a load in three directions. The dimensions of the platens and heel block at different sample  $H/W$  are shown in Fig. 3e–g, respectively. To transfer horizontal principal stress to the rock specimen independently when sample  $H/W$  is 0.5, four heel blocks were prepared to stick to the corresponding horizontal platens. In the case of sample  $H/W$  equal to 1, six platens can be applied to rock surface directly when loading or unloading the principal stress. However, a modified shape platen was used when the sample  $H/W$  2 was tested. This allowed to apply an evenly distributed stress onto the rock specimen during the true-triaxial



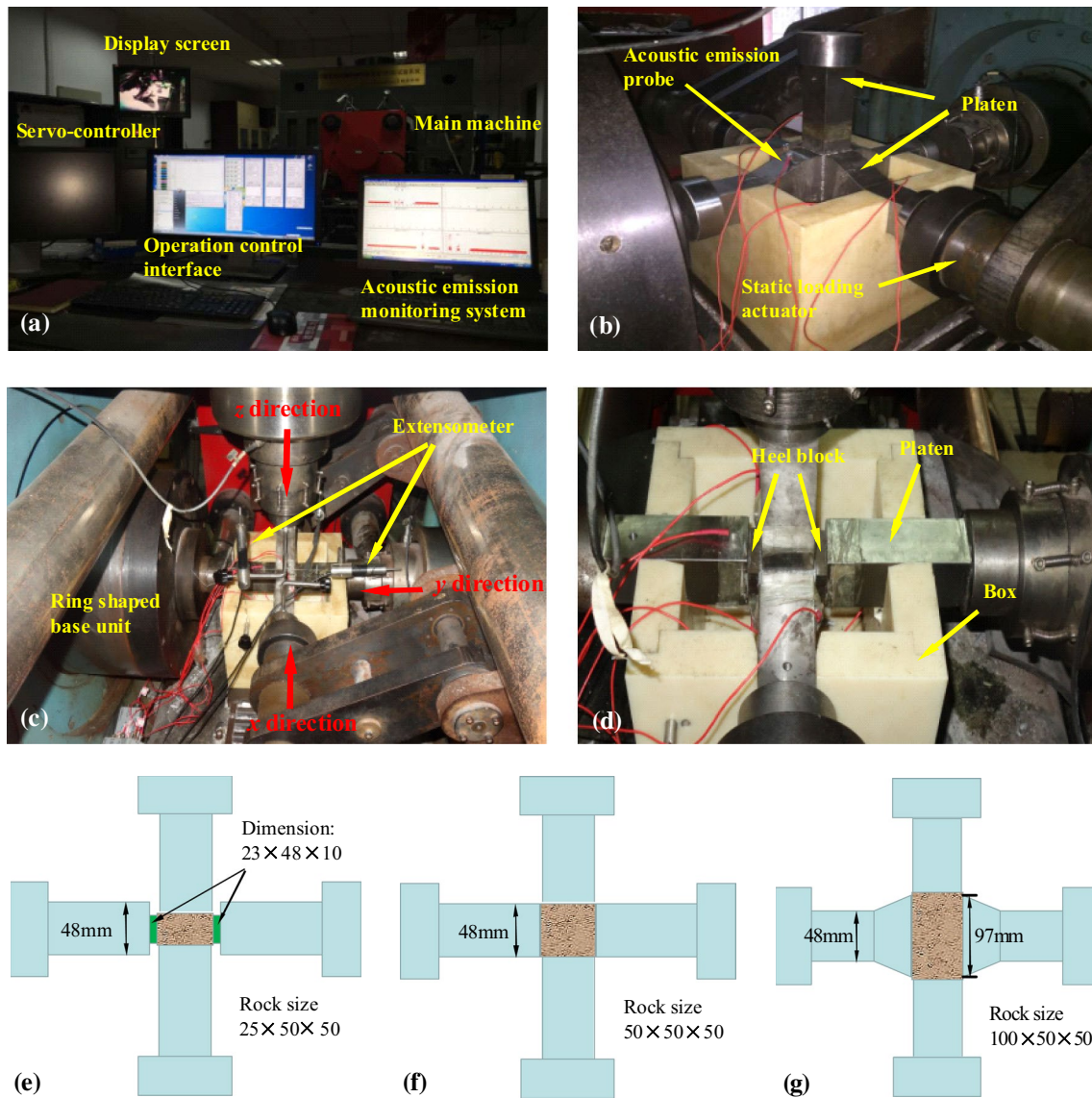


**Fig. 3** Illustration of the true-triaxial test system with a loading apparatus: **a** an overview of the testing system; **b** image of loading apparatus when  $H/W$  is 2; **c** image of loading apparatus when  $H/W$  is 1; **d**

image of loading apparatus when  $H/W$  is 0.5; **e** schematic of loading apparatus when  $H/W$  is 0.5; **f** schematic of loading apparatus when  $H/W$  is 1; **g** schematic of loading apparatus when  $H/W$  is 2

unloading test, as shown in Fig. 3g. All the axial and lateral platens were slightly shorter than the specimen length to allow for rock compression (Haimson and Chang 2000; Ma and Haimson 2016). In addition, butter was used on the six rock surfaces evenly before testing to diminish the frictional resistance from the platens.

### 2.3 Experimental Schemes

The true-triaxial compression tests were divided into three sets corresponding to different  $H/W$  ratios. In each set, the

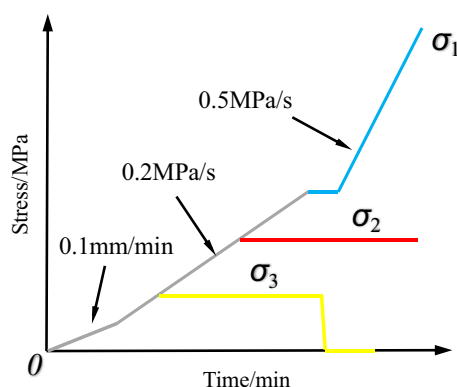
specimens were further divided into three groups according to the ratio of intermediate principal stress to minimum principal stress ( $\sigma_2/\sigma_3$ ): 1.5/1, 2/1, and 3/1. Two samples were used for every test, represented by a and b to ensure the repeatability of the results. Sample serial numbers represent the  $H/W$  and predefined three principal stress ratios, as listed in Table 2. For example, serial number C-10-15-50 means group C,  $H/W$  being 2, 10 indicates the minimum, 15 intermediate, and 50 indicates the predefined maximum principal stress.

The loading and unloading path for a typical sample is shown in Fig. 4, where the loading process in a deep

**Table 2** Rock serial number representing the predefined principle stresses

$\sigma_2/\sigma_3$							
1.5/1	C-10-15-50	C-20-30-50	C-30-45-50	C-40-60-80	C-50-75-100	C-65-100-120	C-80-120-120
	D-10-15-50	D-20-30-50	D-30-45-50	D-40-60-80	D-50-75-100	D-65-100-120	D-80-120-120
	E-10-15-50	E-20-30-50	E-30-45-50	E-40-60-80	E-50-75-100	E-65-100-120	E-80-120-120
2/1	C-10-20-50	C-20-40-50	C-30-60-80	C-40-80-100	C-50-100-120	C-60-120-120	
	D-10-20-50	D-20-40-50	D-30-60-80	D-40-80-100	D-50-100-120	D-60-120-120	
	E-10-20-50	E-20-40-50	E-30-60-80	E-40-80-100	E-50-100-120	E-60-120-120	
3/1	C-10-30-50	C-15-45-50	C-20-60-80	C-25-75-100	C-33-100-120	C-40-120-120	
	D-10-30-50	D-15-45-50	D-20-60-80	D-25-75-100	D-33-100-120	D-40-120-120	
	E-10-30-50	E-15-45-50	E-20-60-80	E-25-75-100	E-33-100-120	E-40-120-120	

The predefined intermediate principle stress is equal to predefined maximum principle stress when the former is larger than 120 MPa in order to avoid abrupt fracturing during unloading due to relatively higher  $\sigma_1$  and  $\sigma_2$

**Fig. 4** Loading and unloading paths during the experimental process

underground working is modeled (Zhao and Cai 2014; Li et al. 2015). Thus, the tangential stress concentration near excavation boundaries can be simulated by gradually increasing  $\sigma_1$  after removal of  $\sigma_3$ , while  $\sigma_2$  remains unchanged throughout the test. Note that even though  $\sigma_2$  may not reach a high value in actual deep underground mine application, perhaps 60 MPa, these high values are indispensable in determining integrated strength values of the rock when  $\sigma_3$  is set to zero to mimic the excavation (stress at failure). In the tests, the maximum principal stress  $\sigma_1$  was in Z direction, the intermediate principal stress  $\sigma_2$ , in Y, and the minimum principal stress  $\sigma_3$ , in X. For testing,  $\sigma_1$  was first raised to 1 MPa under displacement control (0.1 mm/min), then  $\sigma_2$  and  $\sigma_3$  were raised to 0.5 MPa using the same loading regime. After that, a loading speed control of 0.2 MPa/s was utilized to increase the three principal stresses. When  $\sigma_1$  reaches the predefined value,  $\sigma_3$  was removed rapidly to reproduce the excavation unloading process. Subsequently, keeping  $\sigma_2$  constant,  $\sigma_1$  was increased at a loading rate of 0.5 MPa/s to reach the final failure of the rock specimen.

### 3 Experimental Results of Rectangular Prism Specimens Under True-Triaxial Unloading Conditions

#### 3.1 Failure Modes

Figures 5, 6, and 7 present the typical final failure modes of rock specimens under true-triaxial unloading tests with different sample height-to-width ratios and  $\sigma_2/\sigma_3$  ratio of 1.5/1. For longer specimens (100 mm  $\times$  50 mm  $\times$  50 mm), it can be seen from Fig. 5 that the rock specimen failed by shear when the intermediate principal stress ( $\sigma_2$ ) was 15 MPa (C-10-15-50), with a macro-shear band along the diagonal direction. When  $\sigma_2$  was raised to 20 MPa (C-20-30-50), more macrocracks were generated inside the rock specimen of both shear and extensional type, and the final failure mode was dominated by tension with shear (contains both macro-shear and tensile cracks). The specimens are fractured in surface-parallel slabbing failure, only when the  $\sigma_2$  was equal or larger than 45 MPa. In these tests, shear cracks were barely observed in the whole specimen. At sample height-to-width ratios of 1, a similar transition of final failure modes from tension with shear to slabbing could also be observed with the increasing intermediate principal stress under the conditions of the true-triaxial unloading tests. The  $\sigma_2$  value that corresponds to the transformation of failure mode was seen to vary systematically. The failure mode dominated by tension with shear appeared when  $\sigma_2$  was 15 MPa, and the sample  $H/W$  ratio was 1. Slabbing failure appeared when  $\sigma_2$  was equal to or larger than 30 MPa and sample  $W/H$  ratios was 1, which is smaller than the longer specimens. However, the slabbing failure is always the dominant failure mode for all the cases when sample height-to width ratio is 0.5. These results suggest that shorter rock specimens are more prone to produce slabbing failure at smaller intermediate principal stress. For the case where  $\sigma_2/\sigma_3$  was 2/1 and 3/1, the variation regularities of transitional failure modes were analogous





**Fig. 5** Failure modes of specimens in true-triaxial unloading test in Group C with  $\sigma_2/\sigma_3$  being 1.5. *Note:* failure modes of group b are not presented because of similarity and limited space

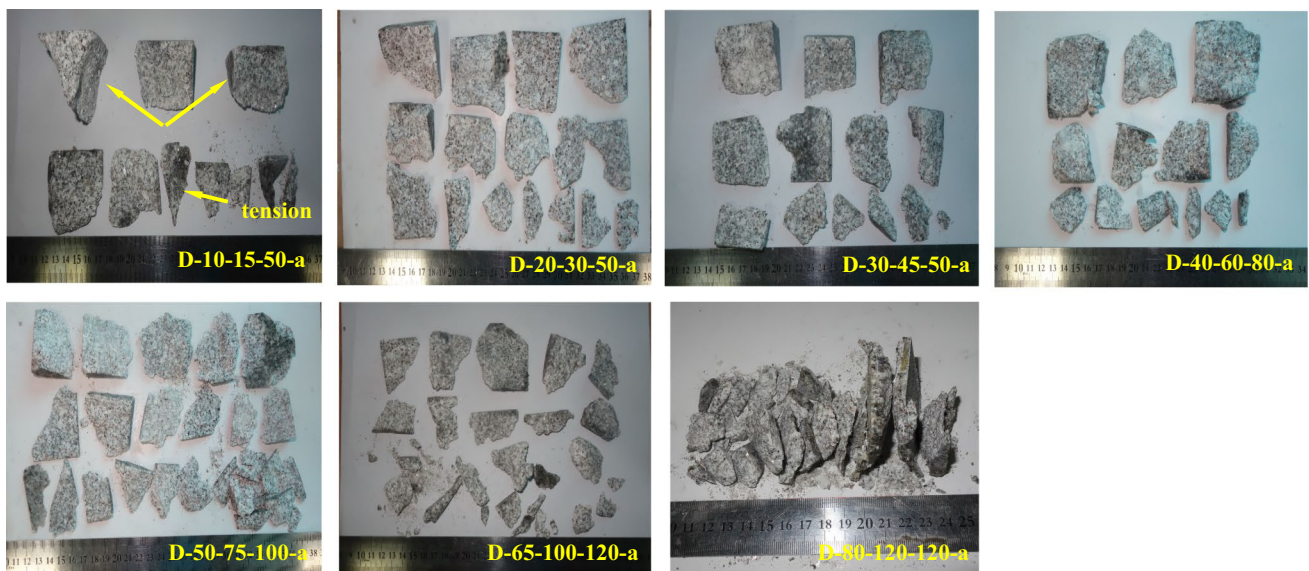


**Fig. 6** Failure modes of specimens in true-triaxial unloading test in Group D with  $\sigma_2/\sigma_3$  being 1.5. *Note:* failure modes of group b are not presented because of similarity and limited space

to the above-mentioned case, and the detailed description of corresponding failure modes will not be conducted in this section. Therefore, it is concluded that the lower the sample height-to-width ratio, the smaller the intermediate principal stress that leads to the occurrence of slabbing failure. Note that the final failure mode was in shear mode for D-10-20-50-a. This might be due to the anisotropy of the rock specimen or uneven stress with improper placement of platens in the direction of  $\sigma_2$ . The failure angle and final failure modes

under the condition of true-triaxial unloading tests are summarized in Table 3.

### 3.2 Stress–Strain Curves and Acoustic Emission Features

To investigate the influence of sample height-to-width ratios and intermediate principal stress on strength characteristics and failure processes (including crack initiation, propagation

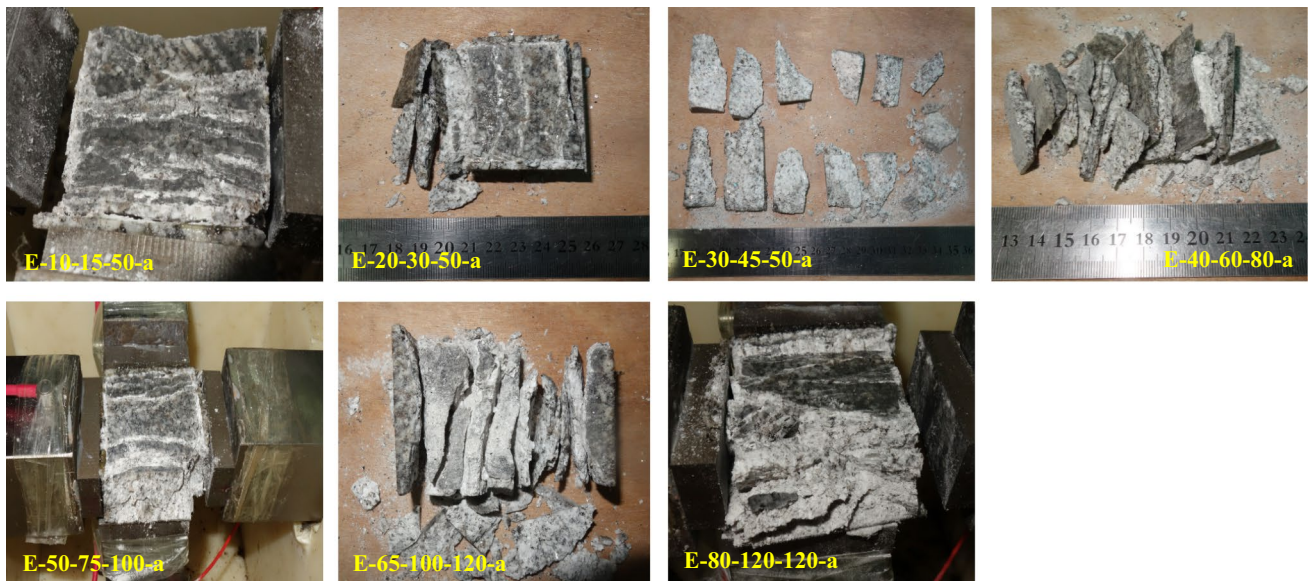


**Fig. 7** Failure modes of specimens in true-triaxial unloading test in Group E with  $\sigma_2/\sigma_3$  being 1.5. *Note:* failure modes of group b are not presented because of similarity and limited space

and coalescence) of granite in true-triaxial unloading tests, the peak unloading strength ( $\sigma_1$  at failure), octahedral shear stress  $\tau_{\text{oct}}$ , effective mean stress  $\sigma_{m,2}$ , AE count rate and cumulative AE energy for all the cases are collected and listed in Table 4. The octahedral shear stress  $\tau_{\text{oct}}$  and effective mean stress  $\sigma_{m,2}$  can be used for establishment of the Mogi–Coulomb failure criterion under true-triaxial conditions and are defined by the following formulae (Mogi 1971a, b; Al-Ajmi and Zimmerman 2005; Chang and Haimson 2012):

$$\tau_{\text{oct}} = \frac{1}{3} \sqrt{(\sigma_1 - \sigma_2)^2 + (\sigma_2 - \sigma_3)^2 + (\sigma_1 - \sigma_3)^2} \quad (1)$$

$$\sigma_{m,2} = (\sigma_1 - \sigma_3)/2$$

where  $\sigma_1$  is the peak strength (stress at failure),  $\sigma_2$  is the intermediate principal stress, and  $\sigma_3$  is the minimum principal stress. Note that the data in Table 4 are the mean values of the two tests. Moreover, the stress–strain curves and the corresponding AE count curves for different sample height-to-width ratios with  $\sigma_2/\sigma_3$  being 2 are also shown in Figs. 8, 9, and 10 for better visualization of failure process and comparison with each other in the following section.

Figure 8 shows the true-triaxial unloading testing results in group C under different intermediate principal stress with  $\sigma_2/\sigma_3$  being 2. It can be seen that the stress–strain curves all present hard and brittle behavior during the entire failure process because of abrupt collapse of peak strength during the final failure. The nonlinear stage before peak strength illustrates the plasticity and ductility of rock that is not easily seen during the entire loading and unloading process for

most rock specimens. This is consistent with the hard and brittle properties of granite and its anticipated behavior. Similar phenomena can also be found in Figs. 9 and 10. The peak unloading strength also experiences a regular variation influenced by the intermediate principal stress. When the intermediate principal stress is increased from 20 to 60 MPa, the peak unloading strength increases monotonically and approaches a maximum value of about 176 MPa, but decreases with further increasing intermediate principal stress. A similar trend in the peak unloading strength is also observed in group D (Fig. 9).

For group E, however, the maximum peak unloading strength was attained only when the intermediate principal stress was equal to 100 MPa, and the value begin to decrease with higher  $\sigma_2$ . For the three rock sizes, the maximum peak unloading strengths (corresponding to  $\sigma_2$  of 60, 60, and 100 MPa in group C, D and E) increased with decreasing sample height-to-width ratios, and the maximum values were 176, 195 and 275 MPa, respectively. For the case of  $\sigma_2/\sigma_3$  equal to 1.5 and 3, the trends observed in Table 4 are analogous to those for  $\sigma_2/\sigma_3$  equal to 2.

During the rock failure process in true-triaxial unloading tests, the maximum AE count and cumulative AE energy were recorded. AE count was plotted in Figs. 8, 9, and 10. AE is extremely sensitive in rock and rock-like materials because of the release of acoustic energy by crack propagation. Taking sample D-10-20-50-a as an example in Fig. 9, the initial increase of AE count was observed when the stress reached 12 MPa (approximately 8% of the peak unloading strength) because of crack closure and compaction. After that, the AE count was stable and constant, with a relatively



**Table 3** Failure angle and final failure modes under true-triaxial unloading tests

Rock number	Failure angle (°)	Failure modes	Rock number	Failure angle (°)	Failure modes	Rock number	Failure angle (°)	Failure modes
C-10-15-50-a	68	Shear	D-10-15-50-a	70, 80	Tension with shear	E-10-15-50-a	82	Slabbing
C-20-30-50-a	70, 80	Tension with shear	D-20-30-50-a	82	Slabbing	E-20-30-50-a	80, 82	Slabbing
C-30-45-50-a	78, 85	Slabbing	D-30-45-50-a	78, 85	Slabbing	E-30-45-50-a	83	Slabbing
C-40-60-80-a	82, 85	Slabbing	D-40-60-80-a	80, 85	Slabbing	E-40-60-80-a	80	Slabbing
C-50-75-100-a	80	Slabbing	D-50-75-100-a	80	Slabbing	E-50-75-100-a	85	Slabbing
C-65-100-120-a	82	Slabbing	D-65-100-120-a	82	Slabbing	E-65-100-120-a	80	Slabbing
C-80-120-120-a	85	Slabbing	D-80-120-120-a	86	Slabbing	E-80-120-120-a	86	Slabbing
C-10-20-50-a	68, 70	Shear	D-10-20-50-a	50, 62	Shear	E-10-20-50-a	80	Slabbing
C-20-40-50-a	70, 85	Tension with shear	D-20-40-50-a	80	Slabbing	E-20-40-50-a	79	Slabbing
C-30-60-80-a	82, 85	Slabbing	D-30-60-80-a	82, 85	Slabbing	E-30-60-80-a	80	Slabbing
C-40-80-100-a	80, 82	Slabbing	D-40-80-100-a	85	Slabbing	E-40-80-100-a	85	Slabbing
C-50-100-120-a	86	Slabbing	D-50-100-120-a	85	Slabbing	E-50-100-120-a	80, 85	Slabbing
C-60-120-120-a	86	Slabbing	D-60-120-120-a	83	Slabbing	E-60-120-120-a	75, 80	Slabbing
C-10-30-50-a	72, 82	Tension with shear	D-10-30-50-a	78, 80	Slabbing	E-10-30-50-a	85	Slabbing
C-15-45-50-a	80, 85	Slabbing	D-15-45-50-a	80	Slabbing	E-15-45-50-a	86	Slabbing
C-20-60-80-a	80, 85	Slabbing	D-20-60-80-a	82	Slabbing	E-20-60-80-a	85	Slabbing
C-25-75-100-a	87	Slabbing	D-25-75-100-a	85	Slabbing	E-25-75-100-a	80	Slabbing
C-33-100-120-a	85	Slabbing	D-33-100-120-a	85	Slabbing	E-33-100-120-a	82	Slabbing
C-40-120-120-a	87	Slabbing	D-40-120-120-a	88	Slabbing	E-40-120-120-a	82, 86	Slabbing

The repeated test results (for example C-10-15-50-b) are not listed due to similarity with previous corresponding data (C-10-15-50-a) and limited space

low value, during the linear elastic stage. The fluctuations of AE count in yield stage imply that the newly generated cracks in granite might be due to both unloading of  $\sigma_3$  and continuous loading of  $\sigma_1$ . The maximum AE count was observed closer the final failure. Comparison between the maximum AE count of granite for different sample-to-height ratios and intermediate principal stress shows no obvious trends under true-triaxial unloading conditions, as can be seen in Table 4. The maximum AE count for all the cases are basically in the range of 22,000–27,000, where the values for shorter specimen were slightly higher than those of taller ones.

Since cumulative AE energy can offer a better reflection of the true energy of an AE event, it can be used to evaluate the energy release characteristics during entire failure process (Zhao et al. 2014). Figure 11 shows the cumulative

AE energy-time history curves for different sample  $H/W$  with  $\sigma_2/\sigma_3$  equal to 2. Note that the unit of cumulative AE energy is “mV” rather than “J” because the recorded data were electrical voltages. It can be seen from Fig. 11a–c that the cumulative AE energy presented the pattern of increase first and decrease subsequently, which is similar to the peak unloading strength characteristics. Moreover, the cumulative AE energy value increased with the decrease in sample height-to-width ratios, with maximum values of 13,602,526, 15,204,006 and 21,773,484 mV, and the latter is significantly higher than the former two. It can be seen in Table 4 that the value for specimen C-20-30-50 was lower than that of specimen C-10-15-50. This might be due to rock heterogeneity or the improper coupling of the acoustic emission probe during experimental preparation.

**Table 4** Test data (mean values) of granite under true-triaxial unloading conditions for different sample *H/W*

Rock number	Predefined principle stress (MPa)			$\sigma_1$ at failure (MPa)	$\tau_{\text{oct}}$ (MPa)	$\sigma_{m,2}$ (MPa)	Max. AE count rate	Cumulative AE energy (mV)
	$\sigma_3$	$\sigma_2$	$\sigma_1$					
C-10-15-50	10 → 0	15	50	152.5	68.62	76.25	23,096	8,972,004
C-20-30-50	20 → 0	30	50	160.2	69.53	80.1	25,007	7,818,142
C-30-45-50	30 → 0	45	50	166	70.09	83	23,071	11,914,177
C-40-60-80	40 → 0	60	80	182.8	76.07	91.4	25,206	13,530,948
C-50-75-100	50 → 0	75	100	156.5	63.03	74.75	24,452	10,357,602
C-65-100-120	65 → 0	100	120	156	64.52	78	24,314	8,789,453
C-80-120-120	80 → 0	120	120	151.3	65.21	75.7	24,078	8,576,943
C-10-20-50	10 → 0	20	50	141.6	62.57	70.8	22,286	8,524,692
C-20-40-50	20 → 0	40	50	152.8	64.69	76.4	24,014	10,225,236
C-30-60-80	30 → 0	60	80	176.2	73.14	88.1	24,565	13,602,526
C-40-80-100	40 → 0	80	100	160.8	65.64	80.4	25,500	10,065,256
C-50-100-120	50 → 0	100	120	146.8	61.22	73.4	24,519	7,563,845
C-60-120-120	60 → 0	120	120	145.8	63.52	75.4	23,976	7,672,093
C-10-30-50	10 → 0	30	50	148	63.88	74	23,830	10,180,116
C-15-45-50	15 → 0	45	50	155.2	65.19	77.6	23,336	11,505,553
C-20-60-80	20 → 0	60	80	174.9	72.56	87.45	24,735	13,481,627
C-25-75-00	25 → 0	75	100	168.4	68.88	84.2	23,486	13,001,246
C-33-100-120	33 → 0	100	120	152.8	63.36	76.4	24,558	10,701,572
C-40-120-120	40 → 0	120	120	147.8	64.13	73.9	24,008	9,335,678
D-10-15-50	10 → 0	15	50	161.2	70.71	80.6	23,721	9,251,159
D-20-30-50	20 → 0	30	50	185.2	77.15	92.6	24,030	12,073,140
D-30-45-50	30 → 0	45	50	178.5	75.79	89.25	24,141	13,557,879
D-40-60-80	40 → 0	60	80	198.6	83.16	99.3	25,074	15,030,024
D-50-75-100	50 → 0	75	100	183.2	75.19	91.6	26,375	14,226,641
D-65-100-120	65 → 0	100	120	173	70.91	86.5	25,106	11,784,510
D-80-120-120	80 → 0	120	120	163.4	69.12	84.2	25,467	10,785,678
D-10-20-50	10 → 0	20	50	153.3	68.04	76.65	23,786	11,728,065
D-20-40-50	20 → 0	40	50	177.1	71.23	83.55	25,068	13,341,620
D-30-60-80	30 → 0	60	80	195.6	81.81	97.8	26,556	15,204,006
D-40-80-100	40 → 0	80	100	179.4	73.38	89.7	26,286	13,551,923
D-50-100-120	50 → 0	100	120	171.2	70.21	85.6	26,880	9,974,623
D-60-120-120	60 → 0	120	120	164.4	69.11	82.2	25,988	9,867,394
D-10-30-50	10 → 0	30	50	175.2	76.50	87.6	23,980	11,829,200
D-15-45-50	15 → 0	45	50	176.8	75.01	88.4	25,013	14,292,614
D-20-60-80	20 → 0	60	80	199.6	83.61	99.8	24,652	16,263,957
D-25-75-00	25 → 0	75	100	189	77.70	94.5	24,166	14,881,957
D-33-100-120	33 → 0	100	120	184.8	75.52	92.4	24,740	12,786,026
D-40-120-120	40 → 0	120	120	173.2	72.45	87.5	25,002	11,988,795
E-10-15-50	10 → 0	15	50	200.2	91.04	100.1	25,313	14,897,778
E-20-30-50	20 → 0	30	50	232	103.02	116	26,533	15,293,031
E-30-45-50	30 → 0	45	50	247.2	107.50	123.6	24,752	17,703,967
E-40-60-80	40 → 0	60	80	240	101.97	120	26,705	17,387,044
E-50-75-100	50 → 0	75	100	258	108.35	129	26,423	20,456,456
E-65-100-120	65 → 0	100	120	286	118.49	143	27,146	22,342,777
E-80-120-120	80 → 0	120	120	251.2	102.58	125.6	26,837	17,144,522
E-10-20-50	10 → 0	20	50	225	101.67	112.5	25,558	15,115,489
E-20-40-50	20 → 0	40	50	233.6	102.00	116.8	26,754	15,518,758
E-30-60-80	30 → 0	60	80	241.6	102.70	120.8	27,965	18,017,125
E-40-80-100	40 → 0	80	100	265	110.97	132.5	27,102	19,665,578

**Table 4** (continued)

Rock number	Predefined principle stress (MPa)			$\sigma_1$ at failure (MPa)	$\tau_{\text{oct}}$ (MPa)	$\sigma_{m,2}$ (MPa)	Max. AE count rate	Cumulative AE energy (mV)
	$\sigma_3$	$\sigma_2$	$\sigma_1$					
E-50-100-120	50 → 0	100	120	275.8	113.99	137.9	27,010	21,773,484
E-60-120-120	60 → 0	120	120	245.6	101.26	122.8	26,522	18,003,081
E-10-30-50	10 → 0	30	50	225.6	100.02	112.8	25,391	15,830,254
E-15-45-50	15 → 0	45	50	240	104.15	120	25,706	18,175,517
E-20-60-80	20 → 0	60	80	254.4	108.57	127.2	26,383	19,069,898
E-25-75-00	25 → 0	75	100	245.6	102.76	122.8	26,589	21,693,846
E-33-100-120	33 → 0	100	120	274.4	113.38	137.2	27,659	22,619,386
E-40-120-120	40 → 0	120	120	240.8	100.30	120.4	27,460	18,263,175

### 3.3 Failure Process

The failure process of granite with different sample height-to-width ratios and predefined principal stresses under true-triaxial unloading conditions were captured and recorded by high-speed camera. To reproduce the fracturing moment and evaluate the degree of damage in hard rocks, a series of selected photos regarding three types of rock sizes with  $\sigma_2/\sigma_3$  equal to 3 are presented in Figs. 12, 13 and 14. Only three stress paths for group C and two stress paths for group D and E are shown for a brief and clear illustration of the failure process.

During the true-triaxial unloading tests, it was observed that the rockburst would occur independent of sample height-to-width ratios and intermediate principal stress. Our experimental results are quite similar to the results of Zhao and Cai (2014). It is worth noting that degree of damage and failure intensity of granite are somewhat distinct for different cases. Figure 12 shows the failure process of granite when sample height-to-width ratio is 2. When the intermediate principal stress is 30 MPa (see Fig. 12a), the localized failures could be observed on the bottom right of the specimen primarily, and the rock fragments are ejected from the unloading face instantly. In such a situation, only a portion of the rock slabs have been splashed from the unloading face. When the intermediate principal stress is increased to 40 MPa, however, the rockburst will occur during the full unloading phase of the face, and the degree of damage would be more severe compared with samples at lower intermediate principal stress (seen in Fig. 12a, b). Note that the failure intensity does not present a monotonically increasing trend with the increase in intermediate principal stress, but reduces after exceeding a critical  $\sigma_2$  value.

The failure processes of granite in groups D and E are shown in Figs. 13 and 14, respectively. In contrast to the taller specimens, when the sample height-to-width ratio is equal to or less than one, the failure areas encompass nearly the full unloading face independent of intermediate principal stress. Moreover, the audible crackling and noises during the

final failure are much more energetic. The failure intensity and degree of damage under true-triaxial unloading conditions are more severe for shorter specimens even when the intermediate principal stress is relatively low (seen in Figs. 13a, 14a).

## 4 Discussion

### 4.1 Influence of Sample $H/W$ Ratio and Intermediate Principal Stress on Transition of Failure Mode

Many studies have attempted to confirm the influence of intermediate principal stresses on the failure modes of rocks or rock-like materials under biaxial and true-triaxial conditions (Mogi 1970, 1971b, 2007; Sahouryeh et al. 2002; Al-Ajmi and Zimmerman 2005; Cai 2008; Li et al. 2015; Du et al. 2015, 2016; Ma and Haimson 2016). By using the true-triaxial compression apparatus, Mogi (1971b) found that the fault plane of Dunham dolomite (with edge ratio of 2:1:1) under true-triaxial loading conditions is fundamentally a nearly flat plane parallel to the  $\sigma_2$  direction, and the fracture angles (between the fracture and the horizontal direction) increase with increasing  $\sigma_2$ . Cai (2008) proposed that the generation of fractures and microcracks (slabbing parallel to the unloading face) that are parallel to tunnel surface can be attributed to the existence of relatively high intermediate principal stress and lower minimum principal stress confinement. In his test, the side length of the prism was 50 mm and the height is 100 mm. Li et al. (2015) observed that the rock failure mode may change from shear to slabbing when  $\sigma_2$  increases to a critical value in a strong and hard rock (cubic specimen of 100 mm length). The main biaxial and true-triaxial compression tests including loading and unloading conditions in history are summarized in Table 5. However, a detailed comparison and analysis indicates that the tested specimens in their experimental procedures were



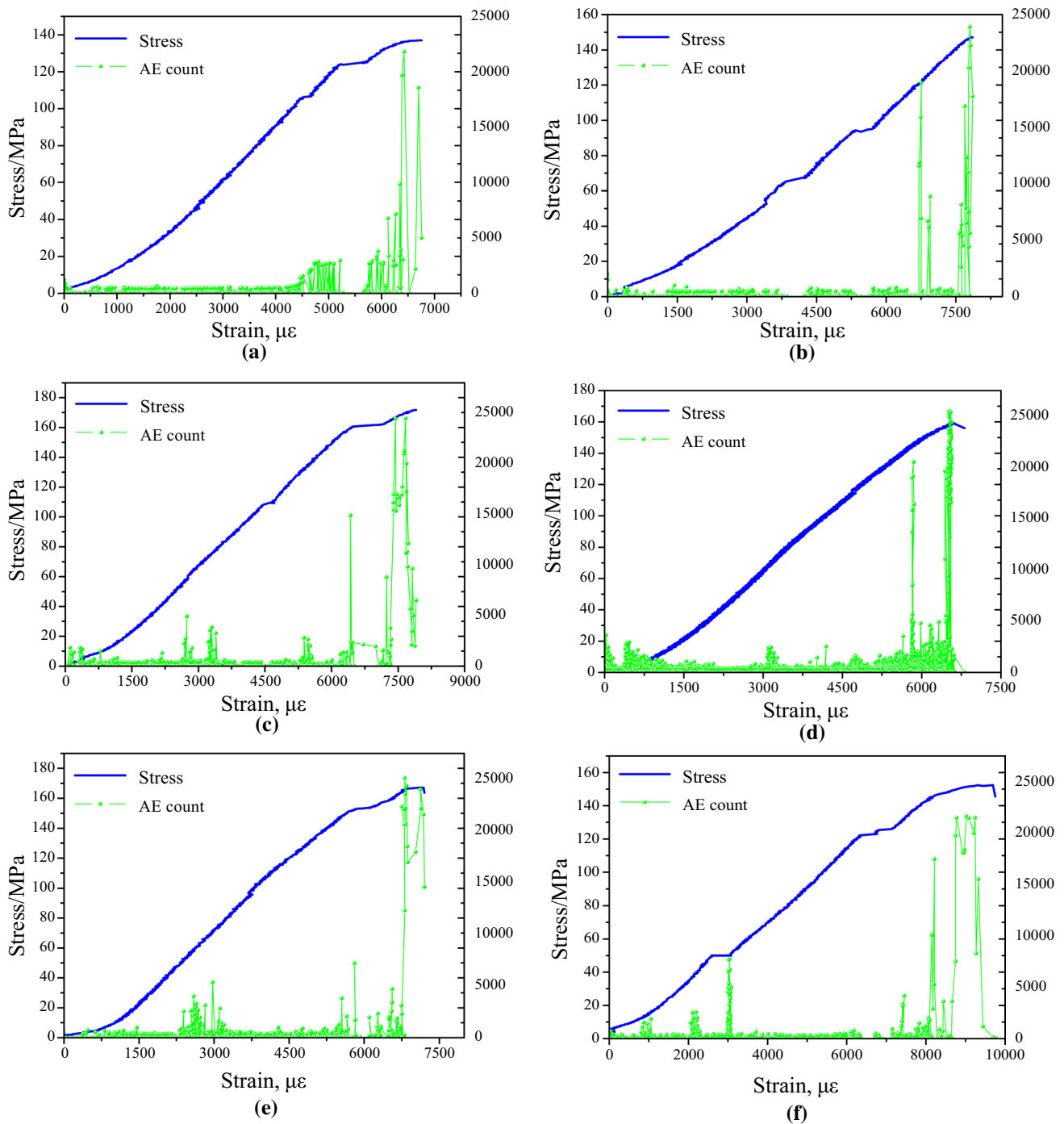


**Fig. 8** The maximum principle stress–strain curves and AE count rate curves in group C with  $\sigma_2/\sigma_3$  being 2. **a** C-10-20-50-b; **b** C-20-40-50-b; **c** C-30-60-80-a; **d** C-40-80-100-a; **e** C-50-100-120-a; **f** C-60-120-120

either rectangular prismatic or cubic specimens; thus, only one type of rock size was considered in their tests. It seems like the impacts of shape effect, especially the sample height-to-width ratio on failure modes of rocks was not taken into account systematically, although the trend of transitional failure modes among the above-mentioned experiments were somewhat analogous.

Other studies have shown the effect of sample size on failure modes of hard rocks under uniaxial and true-triaxial unloading conditions. Li et al. (2011) observed that the failure mode will be transformed from shear to slabbing when the sample height-to-width ratio is reduced to 0.5 in the prism specimens under uniaxial compression. However, their tests did not reflect the excavation

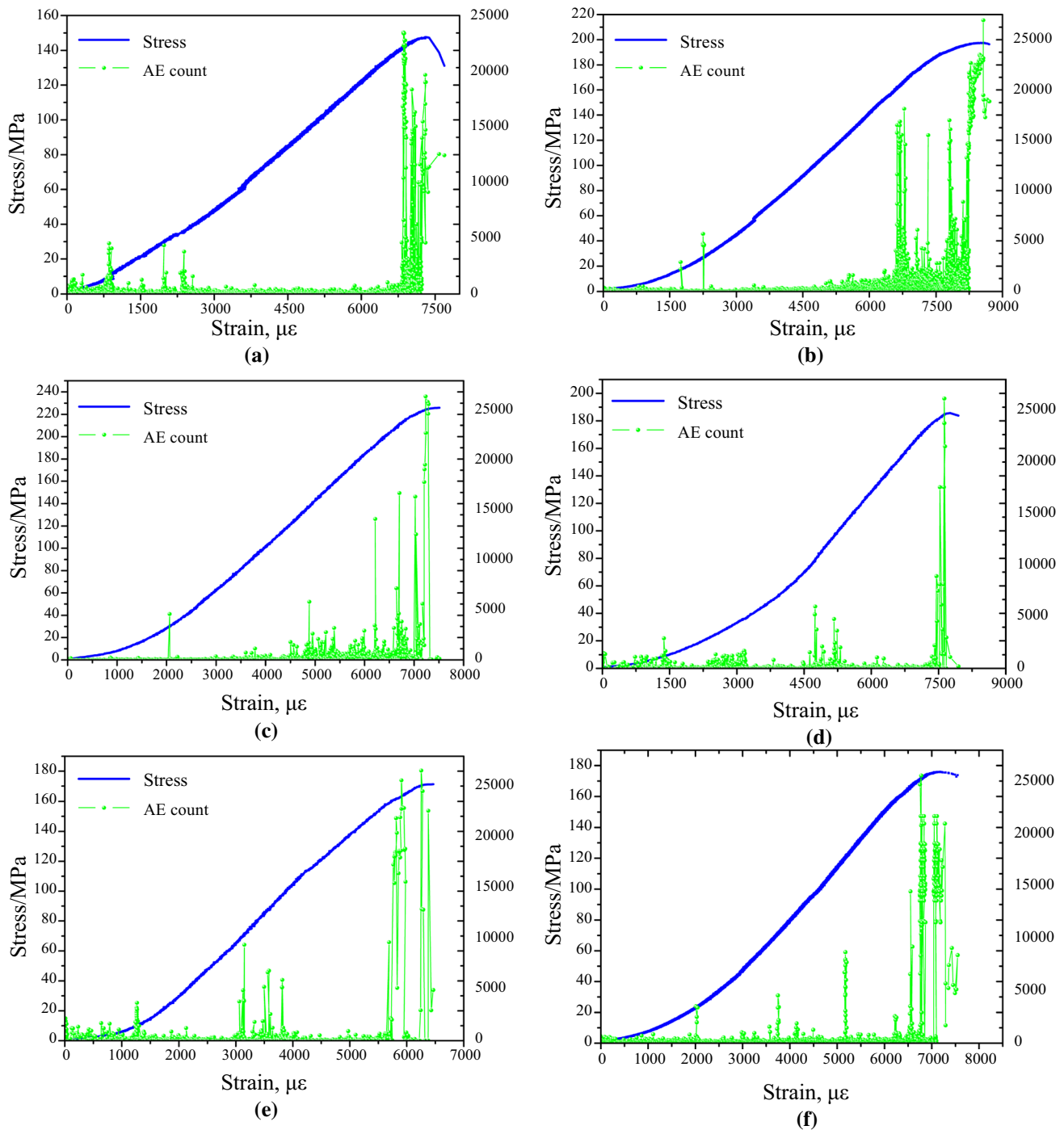


**Fig. 9** The maximum principle stress–strain curves and AE count curves in group D with  $\sigma_2/\sigma_3$  being 2. **a** D-10-20-50-a; **b** D-20-40-50-b; **c** D-30-60-80-b; **d** D-40-80-100-b; **e** D-50-100-120-a; **f** D-60-120-120-b

unloading process in deep underground applications. Zhao and Cai (2014) reported a series of tests that focused on the strainburst characteristics of granite influenced by specimen height-to-width under true-triaxial unloading conditions. Similar experimental research could also be found in Zhao and He (2017). The experimental results

indicated that the dominant failure modes will experience a shift from shear to splitting failures with the increase in height-to-width ratio or height-to-thickness ratio. The different results between previous (Zhao and Cai 2014; Zhao and He 2017) and current research might be due to the following reasons:

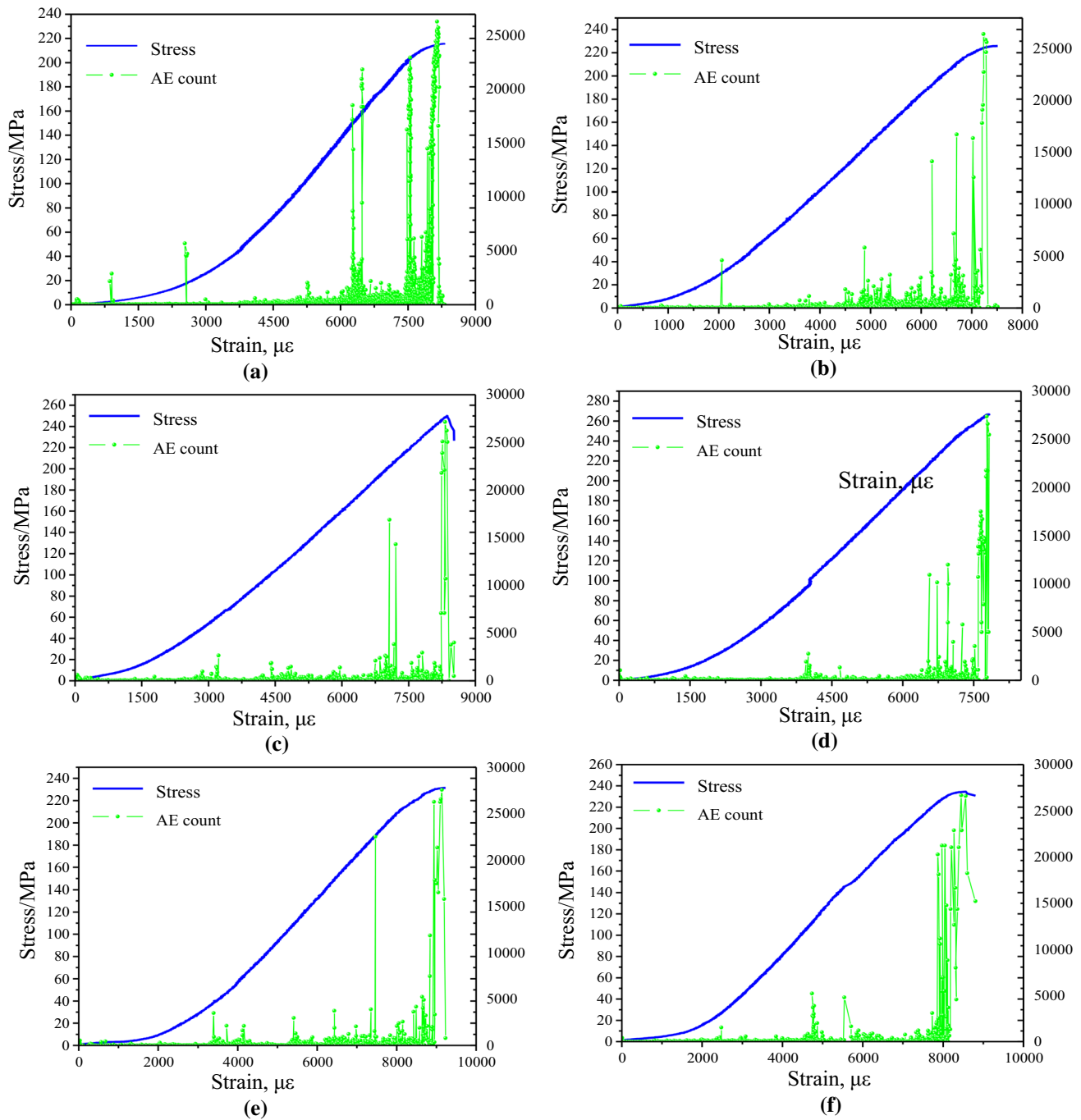


**Fig. 10** The maximum principle stress–strain curves and AE count rate curves in group E with  $\sigma_2/\sigma_3$  being 2. **a** E-10-20-50-a; **b** E-20-40-50-a; **c** E-30-60-80-b; **d** E-40-80-100-a; **e** E-50-100-120-a; **f** E-60-120-120-b

1. In their true-triaxial loading–unloading tests, the influence of intermediate principal stress coupled with sample height-to-width ratios on failure modes of granite was not taken into account. The  $\sigma_2$  value in the two earlier experiments was both approximately 13 MPa, which is lower than our predefined principal stress that is in the range of 15–120 MPa.
2. The sample height-to-width ratios (or sample height-to-thickness ratios) in their tests are equal or greater than 1. The designed sample  $H/W$  in Zhao and Cai (2014) is from 1.0 to 2.5, and the designed sample  $H/T$  in Zhao and He (2017) is in the range of 2.0–5.0. However, the case for sample  $H/W$  equal to 0.5 was not considered in previous true-triaxial tests.



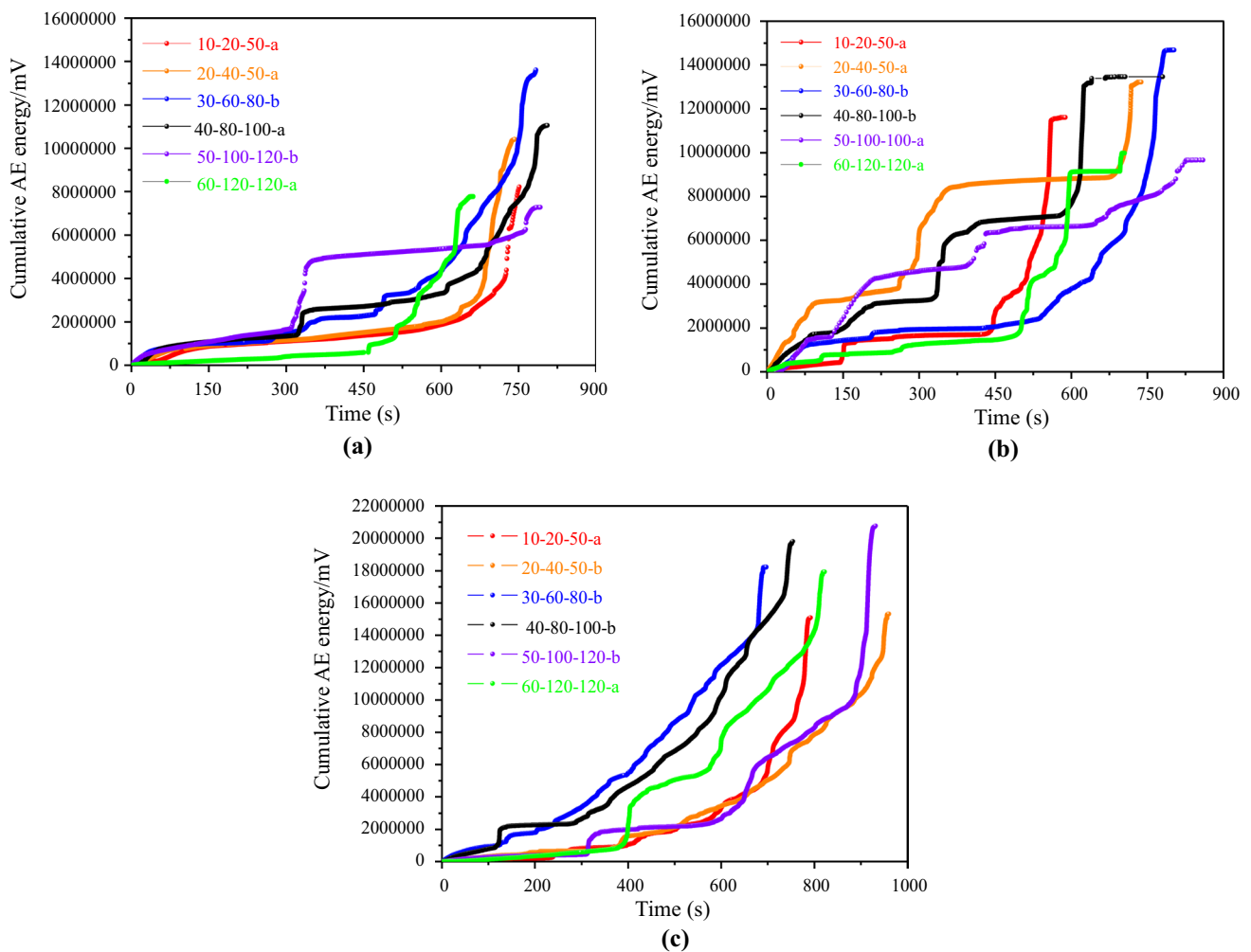


**Fig. 11** The cumulative AE energy-time curves for different sample  $H/W$  with  $\sigma_2/\sigma_3$  being 2. **a**  $H/W = 2$ ; **b**  $H/W = 1$ ; **c**  $H/W = 0.5$

- In the present study, the prepared specimen dimension is 100 mm  $\times$  50 mm  $\times$  50 mm (at a sample width-to-thickness of 1:1), while the dimension of sample width and length in terms of previous two experiments are 60 mm and 30 mm (at a sample width-to-thickness of 2:1). For longer specimens, especially when the height is equal or larger than 120 mm, the specimen  $H/T$  ratio of 4:1 or even greater can be reached. Under such circumstance, the propagation of macrocracks is restricted by limited sample thickness, which might cause the shear failure observed in our test to be viewed as splitting failure in their test.

The determination of failure modes can be based on observation and qualitative analysis. In the present study, another way to investigate failure modes of rock samples, especially for hard rocks, is by analyzing AE data. Acoustic emission monitoring was used in the present study. By analyzing the cumulative AE energy-time curves in Fig. 11,

the failure mode interpretations could be offered. Figure 11a shows the cumulative AE energy-time curves for sample with  $H/W$  of 2 and  $\sigma_2/\sigma_3 = 2$ . Examination of the cumulative AE energy-time curves for samples C-10-20-50-a and C-20-40-50-a shows that they both experienced a long quiet period (also called stable stage), when the cumulative AE energy remained relatively small. This period took approximately 680 s. After that, the cumulative AE energy increases quickly to its peak load till the final sample failure (within 25 s). Similar phenomenon could also be observed in D-10-20-50-a test results (see Fig. 11b). Such evolution trend corresponds to the shear or tension with shear failure under true-triaxial unloading tests. Hence, it is concluded that shear failure can lead to instantaneous collapse for rock strength without obvious pre-warning. However, for the rest of rock samples, the corresponding cumulative AE energy-time curves either experience a series of upward or consistent monotonic increase (especially for sample  $H/W$  of 0.5) during the entire loading and unloading process. This means

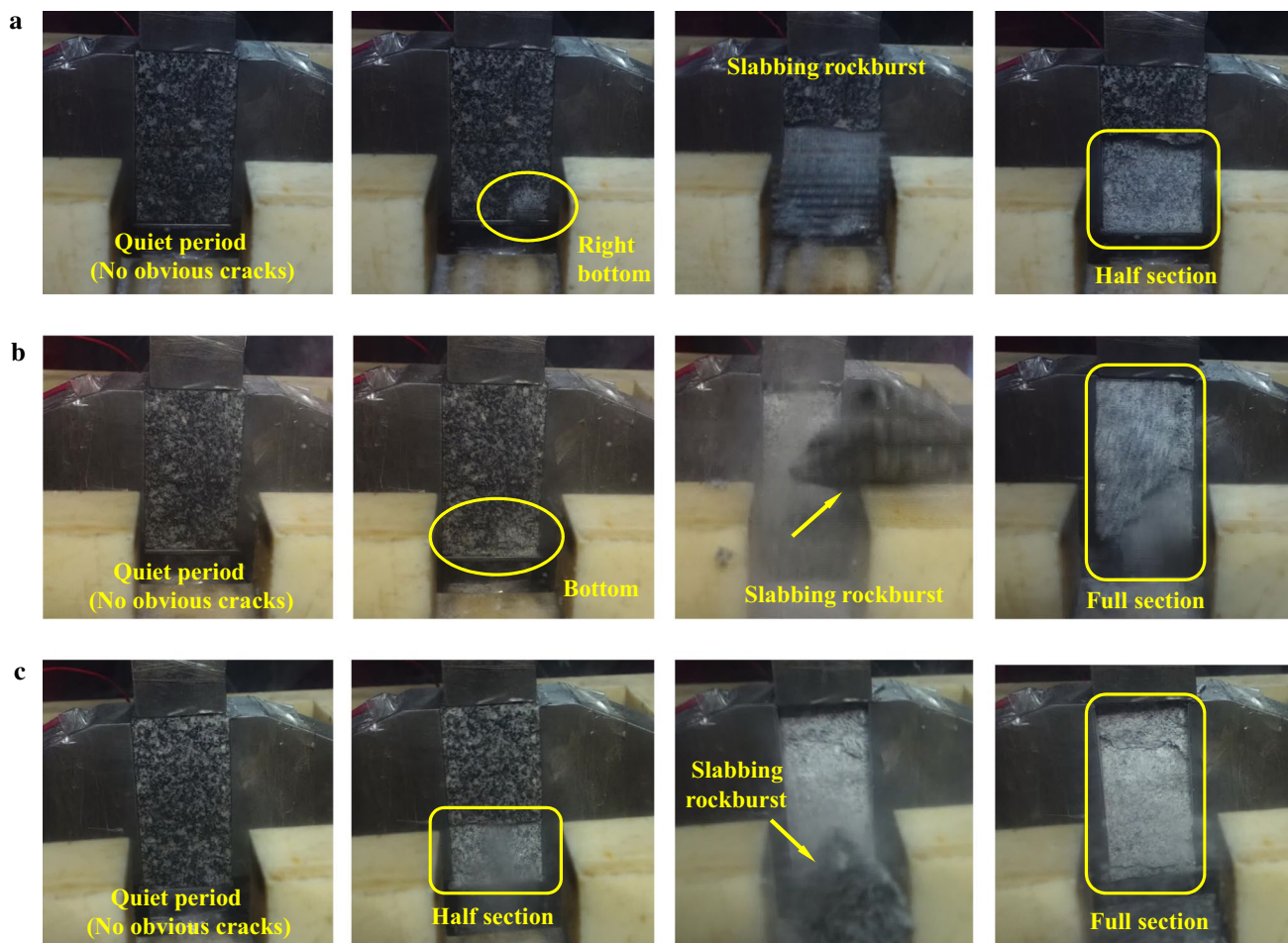


**Fig. 12** Failure process of granite under true-triaxial unloading tests in group C with  $\sigma_2/\sigma_3$  being 3. **a** C-10-30-50-a; **b** C-20-60-80-b; **c** C-33-100-120-a

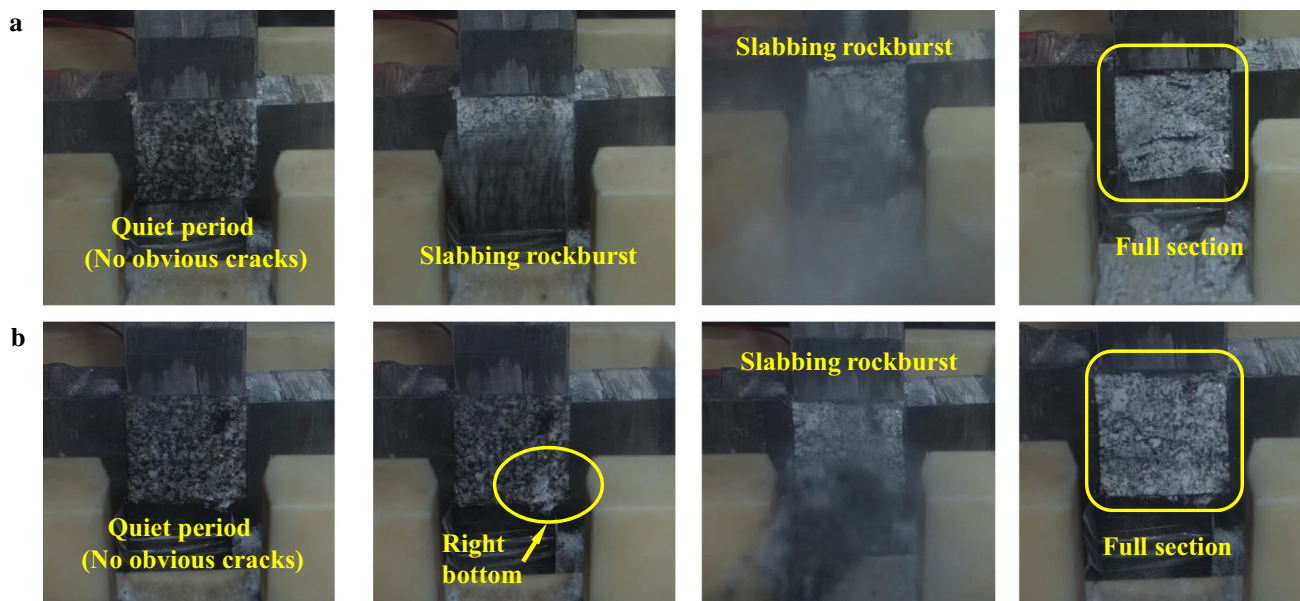


**Fig. 13** Failure process of granite under true-triaxial unloading tests in group D with  $\sigma_2/\sigma_3$  being 3. **a** D-10-30-50-a; **b** D-20-60-80-b

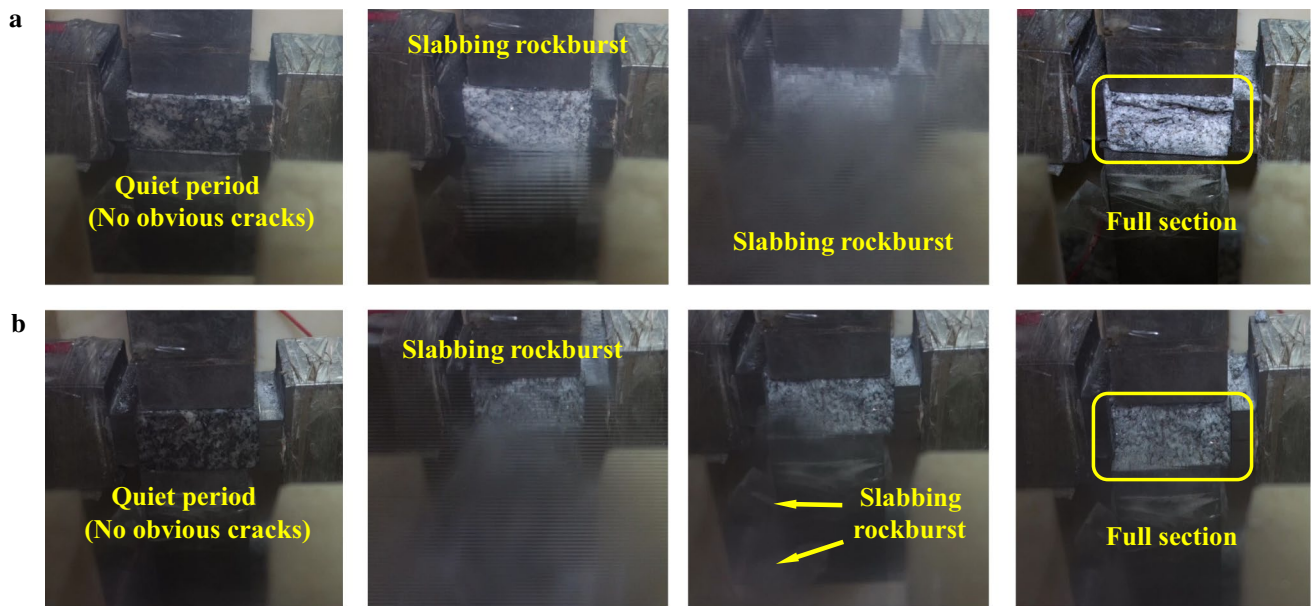


**Fig. 14** Failure process of granite under true-triaxial unloading tests in group E with  $\sigma_2/\sigma_3$  being 3. **a** E-10-30-50-a; **b** E-25-75-100-b

**Table 5** History of primary biaxial and true-triaxial compression tests on rocks and rock-like materials

Type	Specimen dimension (mm)	Rock type	$\sigma_2$ (MPa)	References
True-triaxial loading	15 × 15 × 30	Dunham dolomite, Solnhofen limestone	205–463	Mogi (1971a)
True-triaxial loading	35 × 35 × 70	Sandstone, shale and marble	0–200	Takahashi and Koide (1989)
True-triaxial loading	57 × 57 × 125	Gosford and Castlegate sandstone	100	Wawersik et al. (1997)
True-triaxial loading	19 × 19 × 38	Westerly granite	0–310	Haimson and Chang (2000)
True-triaxial loading	19 × 19 × 38.5	Bentheim and Coconino sandstone	0–620	Ma and Haimson (2016)
True-triaxial loading	100 × 50 × 50	Granite and sandstone	100–350	Feng et al. (2016)
Biaxial loading	100 × 100 × 100	Sandstone, concrete and resin	20–40	Sahouryeh et al. (2002)
Biaxial loading	100 × 50 (3D numerical modeling)	Hard rock	0–10	Cai (2008)
True-triaxial unloading	100 × 50 × 50	Laxiwa granite	15–80	Chen and Feng (2006)
True-triaxial unloading	150 × 60 × 30	Shuicang limestone	60	He et al. (2010)
True-triaxial unloading	150 × 60 × 30	Beishan granite	Lower than 30	Zhao et al. (2014)
True-triaxial unloading	240 × 120 × 120	Cement mortal	–	Zhu et al. (2014)
True-triaxial unloading	100 × 100 × 100	Miluo granite, sandstone and cement mortal	0–40	Li et al. (2015)
True-triaxial unloading	100 × 100 × 100	Miluo granite, Shandong redstone and cement mortal	0–40	Du et al. (2015)
True-triaxial unloading	100 × 100 × 100	Miluo granite, Shandong redstone and cement mortal	20–40	Du et al. (2016)

that the slabbing cracks tend to initiate, propagate and coalesce gradually prior to the peak strength rather than abrupt formation and extension. Since the fractures are parallel to the maximum loading direction, the specimen can still sustain further stress.

In order to illustrate the influence of intermediate principal stress on final failure modes of granite samples, we chose rock samples with height-to-width of 2 as an example

for further comparison and validation of the observations. Figure 15 shows the final failure mode transition of granite influenced by intermediate principal stress in different groups of minimum principal stress. For the case of  $\sigma_3$  being 10 MPa, the failure modes transformed from shear to tension with shear, with shear being the dominant mode of failure when  $\sigma_2$  is less than or equal to 20 MPa. Similarly, for the case of  $\sigma_3$  being 20 MPa, the failure mode remains tension



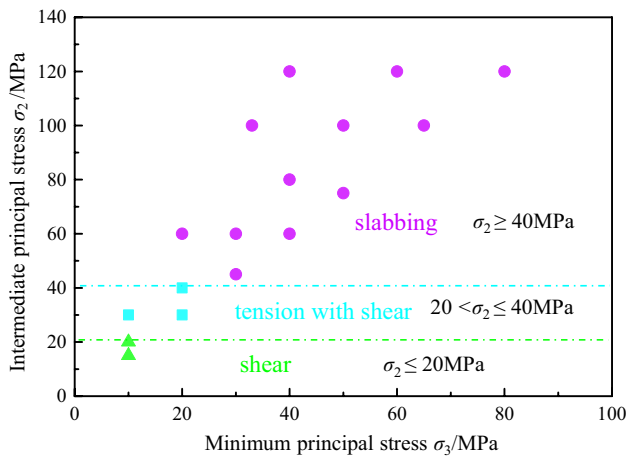


**Fig. 15** Failure modes transition of granite influenced by  $\sigma_2$  in different groups of  $\sigma_3$  with sample height-to-width of 2 under true-triaxial unloading conditions

with shear when  $\sigma_2$  is less than or equal to 40 MPa. With the increase in  $\sigma_2$ , slabbing failure is the dominant failure mode. For the rest of groups, the final failure mode is always the slabbing failure. The reason for the transitional failure modes may be due to higher intermediate principal stress (larger than 45 MPa), rather than higher minimum principal stress (since  $\sigma_3$  will be unloaded to 0 eventually even with a relatively higher value), that leads to the confinement and compression in the  $\sigma_2$  direction that cracks along the  $\sigma_3$  direction are suppressed. Therefore, the specimens are fractured in surface-parallel slabbing failure only when the  $\sigma_2$  is equal or larger than 45 MPa where shear cracks are barely observed in the whole specimen.

Based on our experimental results, it is suggested that the final failure modes of typical hard rocks are the integrated response of intermediate principal stress and sample height-to-width ratio. According to Li et al. (2011) and Brace (1964), many microfractures that are parallel to the loading direction would emerge and propagate along the macro-shear band for longer specimens under a uniaxial compression test, which validated the essence of extension failure in hard rocks. Hence, the failure modes for longer specimens at a very low  $\sigma_2$  are always in shear or in an opposite vertex cone. With the increasing of  $\sigma_2$ , not only the propagation of cracks in the direction of  $\sigma_3$  is suppressed efficiently, but the extensional microcracks that contribute to the macro-shear band subsequently are promoted and motivated to propagate in the direction of  $\sigma_1$ . Figure 16 clearly presents the evolution law of extensional cracks that originated from the shear band when  $\sigma_2$  was increased to 20–40 MPa. It can be seen that the shear band representing the major failure plane tends to disappear when  $\sigma_2$  is equal to 40 MPa. In such cases, the failure mode of granite under true-triaxial unloading condition can be categorized as shear with tension. However, for shorter specimens (with sample  $H/W$

being 1.0 and 0.5), the extensional cracks can easily propagate and develop. This leads to slabbing failure because of limited sample height loaded by  $\sigma_1$  even when the  $\sigma_2$  is lower, which can be seen in Figs. 6 and 7. In brief, the smaller the sample  $H/W$ , the lower the intermediate principal stress that leads to slabbing failure.

#### 4.2 Influence of Sample $H/W$ and Intermediate Principal Stress on Rock Peak Unloading Strength

Though the Mohr–Coulomb criterion has been widely recognized and used in rock mechanics and rock engineering, it does not take into account the effect of intermediate principal stress on rock strength (Al-Ajmi and Zimmerman 2005; Mogi 2007). The von Mises yield criterion considers the effect of  $\sigma_2$  for ductile materials, proposed by Nadai and Hodge (1950), can be expressed by octahedral shear stress (Eq. 1). Nadai indicated that failure would occur when  $\tau_{\text{oct}}$  reaches a critical value. He proposed the following formula:

$$\begin{aligned} \tau_{\text{oct}} &= f(\sigma_{\text{oct}}) \\ \sigma_{\text{oct}} &\equiv \frac{1}{3}(\sigma_1 + \sigma_2 + \sigma_3) \end{aligned} \quad (2)$$

Various failure criteria of this type have been put forward by numerous scholars (Bresler and Pister 1957; Murrell 1965; Sakurai and Serata 1967). Unfortunately, these theories have not improved correlation with the experimental data. Based on comparison with experimental research and theoretical analysis by Mogi (1972), he assumed that the fracture will occur when the distortional strain energy reaches a critical value which increases with the effective mean normal stress  $\sigma_{m,2}$  on the fault plane (see Eq. 1), and the empirical formula is interpreted as:

$$\tau_{\text{oct}} \approx A(\sigma_{m,2})^n \quad (3)$$

where  $A$  and  $n$  are empirical constants. Afterward, several researchers (Haimson and Chang 2000; Chang and Haimson 2012; Lee and Haimson 2011; Al-Ajmi and Zimmerman 2005; Li et al. 2015) validated the proposed failure criterion and confirmed this model, which is considered to be efficient and is known as the Mogi failure criterion. However, lack of a relationship for the parameters appearing in the power-law in Mogi's criterion has been pointed out as a major drawback since it shows little guidance and instruction for application in practical design of underground workings and theoretical research. To correlate Mogi's model with the Coulomb criterion, a linear relationship has been proposed as follows (Al-Ajmi and Zimmerman 2005):

$$\tau_{\text{oct}} = a + b\sigma_{m,2} \quad (4)$$

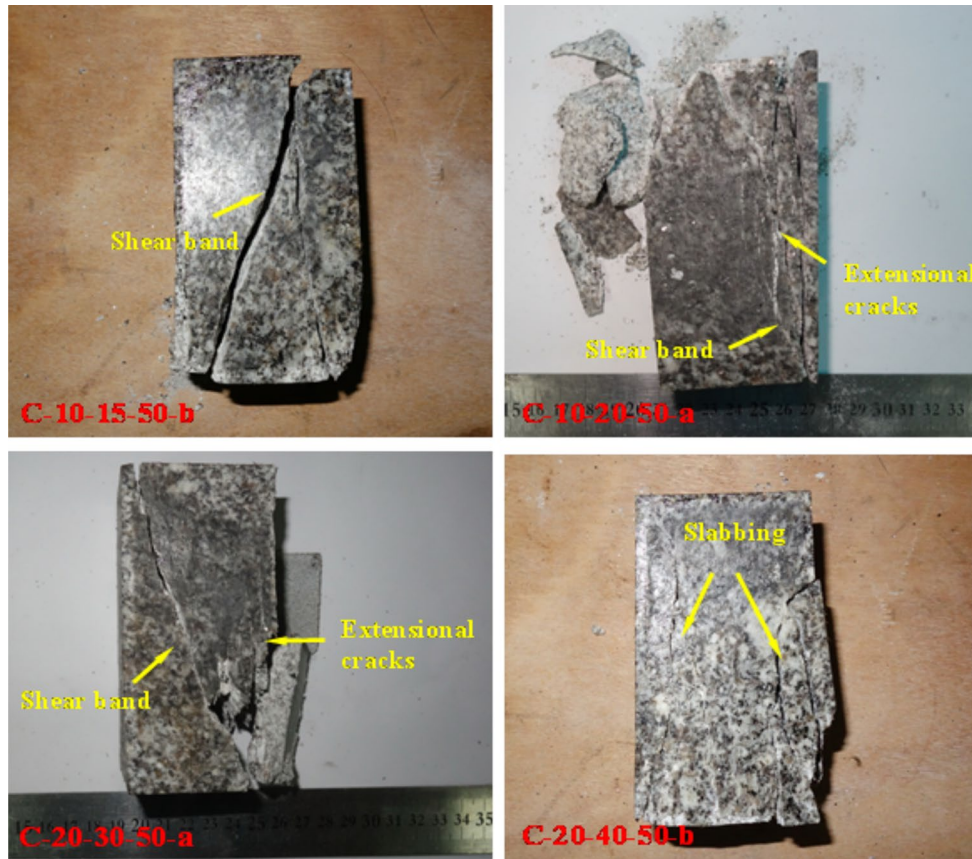


Fig. 16 Transitional process of failure mode from shear to slabbing for typical rock specimens in group C

where  $a$  is the intersection of the failure envelope line with the  $\tau_{oct}$ -axis, and  $b$  is inclination or slope of the line. Since the linear Mogi criterion is linked to the Coulomb criterion (also known as Mogi–Coulomb criterion), the relationship can be expressed as follows:

$$a = \frac{2\sqrt{2}}{3}C \cos \varphi, \quad b = \frac{2\sqrt{2}}{3} \sin \varphi \tag{5}$$

where  $C$  is the cohesion and  $\varphi$  is the angle of internal friction of the material. In numerical calculations (Al-Ajmi and Zimmerman 2005), the Mogi–Coulomb criterion has been verified to represent rock failure under true-triaxial loading states as well as the power-law form, and the usefulness of the Mogi failure criterion can be verified as well.

It is noteworthy that the true-triaxial failure criteria were all based on true-triaxial loading tests in previous works, except for Li et al. (2015). To clarify the applicability of the Mogi–Coulomb criterion in true-triaxial unloading conditions, we present the stress  $\sigma_1$  at failure point as function of  $\sigma_2$ , and the  $\tau_{oct}$  as function of  $\sigma_{m,2}$  in the form of Eq. (4) for different sample height-to-width

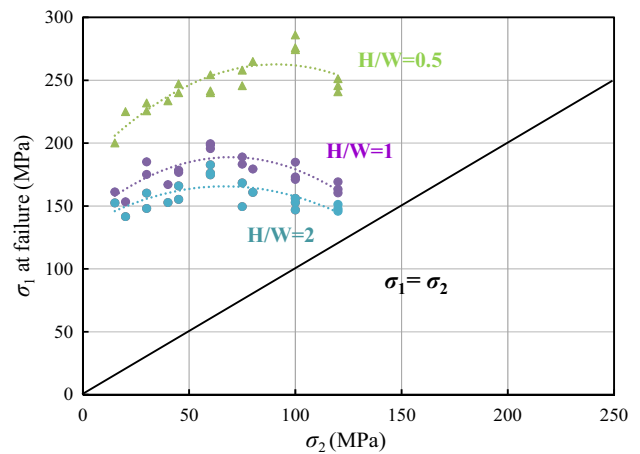
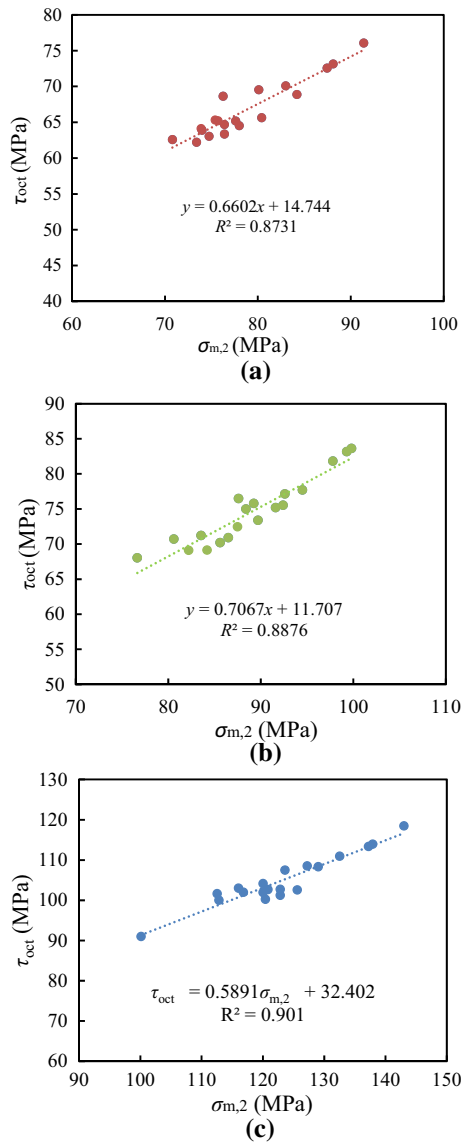


Fig. 17 The maximum principal stress ( $\sigma_1$ ) at failure as functions of  $\sigma_2$  for different sample  $H/W$  under true-triaxial unloading conditions. Note: the dotted lines indicate the fitting curves of peak strength by a polynomial equation



**Fig. 18** The octahedral shear stress ( $\tau_{oct}$ ) at failure as functions of effective mean normal stress ( $\sigma_{m,2}$ ) for different sample  $H/W$  under true-triaxial unloading conditions. **a**  $H/W = 2$ ; **b**  $H/W = 1$ ; **c**  $H/W = 0.5$ . *Note:* the dotted lines indicate the fitting curves of octahedral shear stress as functions of effective mean stress based on Mogi–Coulomb failure criterion

ratios under true-triaxial unloading conditions, as can be seen in Figs. 17 and 18.

Generally, much attention has been paid to the development of models of true-triaxial loading strength under higher intermediate principal stress. In the present study, the predefined  $\sigma_2$  value in the range of 15–120 MPa was considered comprehensively under true-triaxial loading–unloading state. It can be seen from Fig. 16 that independent of sample  $H/W$  ratio, the peak unloading strengths ( $\sigma_1$  at failure) present a pattern of increase at the beginning of the loading cycle and decrease subsequently, instead of a monotonic increase. It can be seen that the evolution of unloading strength in our results is similar to that in true-triaxial loading tests where the intermediate principal stress is in the range of  $\sigma_3 \leq \sigma_2 \leq \sigma_1$ . For the case of sample  $H/W$  being 2, 1 and 0.5, the peak unloading strengths begin to deviate at a  $\sigma_2$  of 60, 60 and 100 MPa, respectively. Moreover, the peak unloading strength increases with the decreasing sample  $H/W$  ratio. For practical underground engineering applications, this means that rock fragmentation and mining activities may be more difficult with lower roadway heights, when excavating a tunnel or stope in the orebody.

Figure 18 presents the fitted curves of  $\tau_{oct}$  as function of  $\sigma_{m,2}$  for different sample height-to-width ratios by using the linear Mogi criterion. The  $a$  and  $b$  values are 14.744 and 0.6602 for group C, 11.707 and 0.7067 for group D and 32.402 and 0.5891 for group E, respectively. Therefore, the corresponding  $C$  and  $\varphi$  could also be calculated according to Eq. (5). Table 6 presents the calculated material parameters based on Mogi–Coulomb criterion and Mogi criterion. From the correlation coefficient values ( $R^2$ ), it was found that the linear form does as good a job as the power-law form in fitting the data. Note that the correlation coefficient values are 0.8645 and 0.8774 for the case of sample  $H/W$  equal to 2 and 1, respectively, if employing the power-law failure envelopes, which is even lower compared with linear model. According to the goodness of fit, it can be concluded that Mogi–Coulomb failure criterion can be applied to hard rocks and may do well in evaluating failure characteristics under true-triaxial unloading states.

In Fig. 19, unloading peak strength of various  $\sigma_2/\sigma_3$  values is plotted for all considered sample  $H/W$  ratios. It seems the peak unloading strength is not influenced by the ratio of intermediate principal stress to minimum principal stress ( $\sigma_2/\sigma_3$ ), since the entire variation trend of strength, deemed

**Table 6** The calculated material parameters based on Mogi–Coulomb criterion and Mogi criterion

Sample $H/W$	Mogi–Coulomb criterion		Mogi criterion			$A$	$n$	$R^2$
	$a$	$b$	$C$ (MPa)	$\varphi$ (°)	$R^2$			
2/1	14.744	0.6602	21.8	44	0.8731	2.8582	0.7211	0.8645
1/1	11.707	0.7067	18.7	48.5	0.8876	3.5329	0.682	0.8774
0.5/1	32.402	0.5891	42.5	36.1	0.901	4.201	0.6684	0.9073



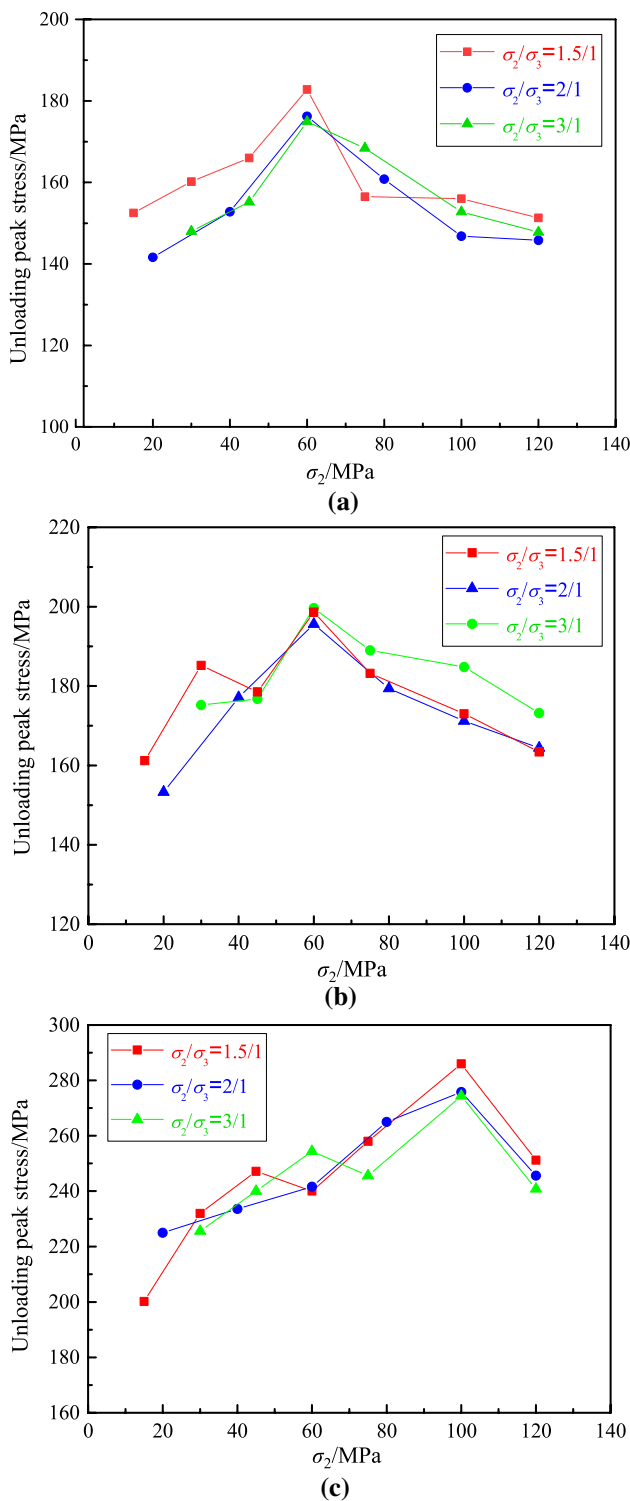


**Fig. 19** Unloading peak strength of different  $\sigma_2/\sigma_3$  values as functions of intermediate principal stress for three types of sample height-to-width ratios: **a**  $H/W = 2$ ; **b**  $H/W = 1$ ; **c**  $H/W = 0.5$

as ascending-then-descending, as functions of intermediate principal stress is identical generally, even the slight fluctuation would occur with  $\sigma_2/\sigma_3$  being 1.5 when  $\sigma_2$  is less than

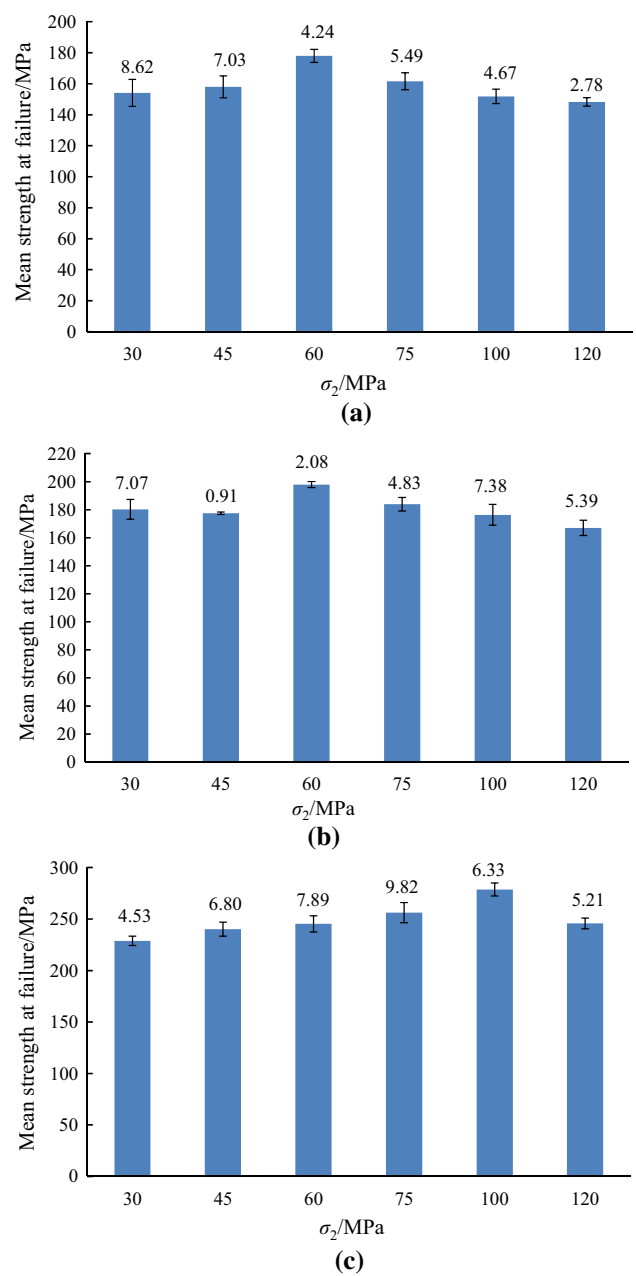


**Fig. 20** Average peak unloading strength and the corresponding standard deviation value of rock specimens in different groups. Each group represents the case of different  $\sigma_3$  for a constant  $\sigma_2$ : **a**  $H/W$  is 2; **b**  $H/W$  is 1; **c**  $H/W$  is 0.5. Note: the condition of  $\sigma_2$  being 45 and 40, 75 and 80 MPa are integrated into one group respectively due to numerical adjacency

60 MPa in lower samples ( $H/W = 1$  and  $0.5$ , in Fig. 19b, c). Figure 20 shows the average peak unloading strength and the corresponding standard deviation value of three types of rock specimens in different groups. Each group represents the different  $\sigma_3$  for a constant  $\sigma_2$ . Note that the condition of  $\sigma_2$  being 45, 40, 75, and 80 MPa are integrated into one group, respectively, due to numerical similarity. The small

standard deviation of average unloading strength, ranging from 0.91 to 9.82, indicates that the true-triaxial unloading strength remains the same for a constant  $\sigma_2$  irrespective of the minimum principal stress. Similar variation trend could also be observed by comparison of final failure modes of granite under true-triaxial unloading conditions. It can be inferred from Table 3 that, for the samples with similar  $H/W$  ratio, the final failure modes are basically the same for a constant  $\sigma_2$ , no matter what the  $\sigma_2/\sigma_3$  values are. In other words, for a given intermediate principal stress, the minimum principal stress has little influence on the failure characteristics of granite under true-triaxial unloading conditions.

Increasing the boundary shear (between the specimen and the loading platen) or decreasing the sample height-to-width ratio will yield a higher peak stress because of the end friction or size effect, although lubricant and copper shims are used to eliminate the additional confinement due to six specimen face metal spacers used in the polyaxial loading and unloading system (Haimson and Chang 2000; Cai 2008; Manouchehrian and Cai 2015). Therefore, for those specimens in the true-triaxial unloading test, especially for the case of sample with  $H/W$  of 0.5, the peak unloading stress will be slightly higher than the true values. Du et al. (2015) investigated the rock failure characteristics under true-triaxial unloading conditions. In their tests, the cubic rock specimens, with  $H/W$  ratio of 1, were used to accommodate the Model TRW-3000 testing machine. By detailed comparison and analysis, it was found that the end effect caused by the  $H/W$  ratio of 1 for the cubic specimens will not significantly affect the testing results under true-triaxial tests. Therefore, it is suggested that the critical value of sample  $H/W$  ratio to be used to obtain the real rock strength should be at least 1. Further numerical and experimental studies are still needed to investigate the influence of size effect and intermediate principal stress on strength characteristics under true-triaxial unloading states, in which the end friction could be eliminated thoroughly.

### 4.3 Influence of Sample $H/W$ Ratio and Intermediate Principal Stress on Severity of Rockburst

In recent years, a series of intense rockburst events has occurred in deep, highly stressed, hard rocks which have led to casualties, damage to the machinery and significant economic losses (Zhang et al. 2015). Rockburst has been a focus in the field of rock mechanics and rock engineering. Zhao et al. (2014) proposed that the degree of violence during rock fracturing is related to the unloading rate. Hard rocks are more prone to induce slabbing rockburst at higher unloading rates, while they are more susceptible to slabbing or spalling failure at lower unloading rates. Therefore, it has been suggested by some researchers (Feng et al.

2017) that slabbing is also a precursor for strain rockburst. Based on the description and definition by Ortlepp and Stacey (1994), Kaiser and Cai (2012) divided rockburst into strainburst, pillar burst, and fault-slip burst. Of these categories, strainburst is the most common form observed in the laboratory or at underground sites. In the present study, the slabbing rockburst can be classified as strainburst (He et al. 2010). The severity of strainburst is strictly dependent on the strain energy stored in hard rocks since the failure process is accompanied by energy dissipation and release of elastic strain energy (Xie et al. 2005). If the stored elastic strain energy is larger than the surface energy required for fragmentation of hard rocks, failure will occur, even if the rockburst is induced by excess kinetic energy. The stored strain energy is closely related to the predefined principal stress, especially the intermediate principal stress under true-triaxial unloading conditions. To evaluate the released energy characteristics and intensity of rockburst during rock failure, the cumulative AE energy is collected and listed in Table 4. Plot of the corresponding cumulative AE energy values under different sample  $H/W$  ratios and intermediate principal stress  $\sigma_2$ , is offered in Fig. 21.

It can be seen in Fig. 21 that the cumulative AE energy under different sample  $H/W$  ratios present a pattern of increase, followed by a decrease in magnitude which is quite similar to that of peak unloading strength as functions of intermediate principal stress. Combined with the previous strength results, it can be concluded that while the specimens in group E have a higher bearing capacity compared to taller specimens (groups C and D), the failure intensity is the most violent and severe. During excavation of a lower roadway or tunnels in underground mines, the probability of rockburst can be minimized while the severity could be increased. Therefore, it is necessary to take proper steps to strengthen

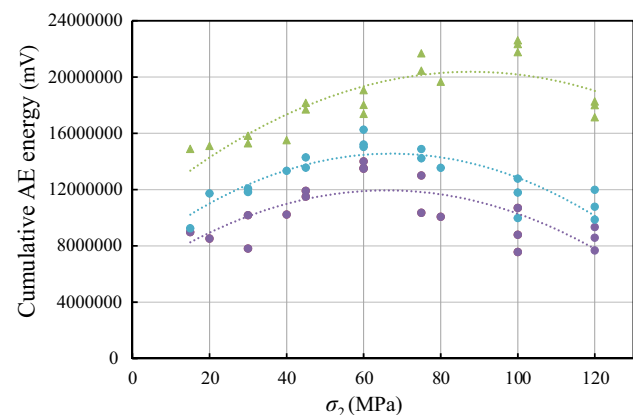


**Fig. 21** The cumulative AE energy as functions of  $\sigma_2$  for different sample  $H/W$  under true-triaxial unloading conditions. *Note:* The dotted lines indicate the fitting curves of cumulative AE energy by a polynomial equation

the support measures in sidewalls or roofs of roadway to be proactive in preventing the rockburst. Conversely, the supporting strategies for higher roadway or tunnel should be different and targeted. Since the higher probability and lower severity of rockburst occurs in these openings, a real-time monitoring system and timely ground support installation are critical to establish an efficient support scheme that is both secure and economical. It is noteworthy from Fig. 21 that the intermediate principal stress also plays an important role in the severity of rockburst. The cumulative AE energy showed a monotonically increasing trend in a certain range and may reflect the increasing intensity of rockburst because of the stored elastic strain energy confined by  $\sigma_2$  and unloading by  $\sigma_3$ . The cracks in hard rocks are initiated and propagate, however, if  $\sigma_2$  continues to increase, which triggers the transition from intact hard rocks to fractured rock mass, the stored energy may dissipate. In the present study, the corresponding  $\sigma_2$  for different sample  $H/W$  ratios at which both peak unloading strength and cumulative AE energy (representing the rockburst severity) deflect are 60, 60 and 100 MPa. Note that the failure process depicted by high-speed images in Sect. 3.3 is identical to the experimental results of AE data.

## 5 Conclusion

The influence of sample  $H/W$  ratios and intermediate principal stress on failure characteristics of granite under true-triaxial unloading conditions was studied and investigated in the present study. Three rock sizes with sample  $H/W$  of 2, 1 and 0.5 were prepared, and a loading apparatus coupled with a true-triaxial unloading system is also designed for samples of various dimensions. Research results indicate that shorter rock specimens can produce slabbing failure even with smaller intermediate principal stress while higher intermediate principal stress for longer specimens. The corresponding  $\sigma_2$  values that trigger the occurrence of slabbing failure for Miluo granite are 45, 30 and 15 MPa as the sample  $H/W$  decreases from 2 to 0.5. It was observed that increasing  $\sigma_2$  not only does suppress the crack propagation in the direction of  $\sigma_3$ , but also expedites the extension of microcracks in the direction of  $\sigma_1$  and  $\sigma_2$ . The limited sample height in shorter specimens may contribute to the lower  $\sigma_2$  for the transition of failure mode because the microcracks can easily propagate and coalesce. The peak unloading strength as a function of  $\sigma_2$  for different sample  $H/W$  ratios present the pattern of an initial increase, followed by a decrease with the intermediate stress  $\sigma_2$ . Moreover, the peak unloading strength increases with the reduction in sample height. The results of this study validated the applicability of the Mogi–Coulomb failure criterion for evaluating failure characteristics under true-triaxial unloading conditions. The time history

of rockburst severity expressed by high-speed images and cumulative AE energy monitoring during the failure process showed to be consistent with that of peak unloading strength. Some suggestions are given for roadway support during excavation of deep underground workings that could safeguard against rockburst events and reduce their negative impacts. Moreover, current experimental results confirm that different  $\sigma_2/\sigma_3$  values (i.e. 1.5, 2 and 3), for a constant  $\sigma_2$ , have little influence on failure characteristics of granite, indicating the independence of minimum principal stress on the failure process of hard rocks. Based on the experimental results in this study, it is concluded that the failure characteristics of typical (homogeneous) hard rocks are the integrated response of intermediate principal stress and sample height-to-width ratio under true-triaxial loading–unloading conditions. Further numerical research by using combined FEM/DEM approach is still needed to further validate these results. Also, the condition of static–dynamic coupled loading under true-triaxial conditions should be the focal point of a follow up study.

**Acknowledgements** The authors would like to acknowledge the financial supports from the State Key Research Development Program of China (Grant Number 2016YFC0600706) and the National Natural Science Foundation of China (Grant Numbers 51474250, 51504287).

## References

- Al-Ajmi AM, Zimmerman RW (2005) Relation between the Mogi and the Coulomb failure criteria. *Int J Rock Mech Min Sci* 42:431–439
- Alexeev A, Revva V, Bachurin L, Prokhorov I (2008) The effect of stress state factor on fracture of sandstones under true triaxial loading. *Int J Fract* 149:1–10
- Bažant ZP, Xiang Y (1997) Size effect in compression fracture: splitting crack band propagation. *J Eng Mech* 123:207–213
- Besuelle P, Hall SA (2011) Characterization of the strain localization in a porous rock in plane strain condition using a new true-triaxial apparatus. In: Bonelli S, Dascalu C, Nicot F (eds) *Advances in bifurcation and degradation in geomaterials*. Springer, New York, pp 345–352
- Blake W, Hedley DGF (2003) *Rockbursts: case studies from North American hard-rock mines*. SME, Colorado
- Brace WF (1964) Brittle fracture of rocks. In: Judd WR (ed) *State of stress in the Earth's crust, Proceedings of the international conference, Santa Monica, America*. Elsevier, New York, pp 110–178
- Bresler B, Pister KS (1957) Failure of plain concrete under combined stresses. *Trans Am Soc Civ Eng* 122:1049–1068
- Cai M (2008) Influence of intermediate principal stress on rock fracturing and strength near excavation boundaries—insight from numerical modeling. *Int J Rock Mech Min Sci* 45:763–772
- Chang C, Haimson BC (2000) True triaxial strength and deformability of the German Continental Deep Drilling Program (KTB) deep hole amphibolite. *J Geophys Res Solid Earth* 105:18999–19013. <https://doi.org/10.1029/2000JB900184>
- Chang C, Haimson BC (2012) A failure criterion for rocks based on true triaxial testing. *Rock Mech Rock Eng* 45:1007–1010

- Chen JT, Feng XT (2006) True triaxial experimental study on rock with high geostress. *Chin J Rock Mech Eng* 25:1537–1543 (in Chinese)
- Diederichs MS (2007) The 2003 Canadian geotechnical colloquium: mechanistic interpretation and practical application of damage and spalling prediction criteria for deep tunneling. *Can Geotech J* 44:1082–1116
- Dreyer W, Borchert H (1961) Zur druckfestigkeit von salzgesteinen. *Kali und Steinsalz* 3:234–241
- Du K, Li XB, Li DY, Weng L (2015) Failure properties of rocks in true-triaxial unloading compressive test. *Trans Nonferrous Met Soc China* 25:571–581
- Du K, Tao M, Li XB, Zhou J (2016) Experimental study of slabbing and rockburst induced by true-triaxial unloading and local dynamic disturbance. *Rock Mech Rock Eng* 49:3437–3453
- Duan K, Kwok CY, Ma X (2017) DEM simulations of sandstone under true triaxial compressive tests. *Acta Geotech* 12(3):495–510
- Feng XT, Zhang XW, Kong R, Wang G (2016) A novel Mogi type true triaxial testing apparatus and its use to obtain complete stress–strain curves of hard rocks. *Rock Mech Rock Eng* 49:1649–1662
- Feng F, Li XB, Li DY, Wang SF (2017) Research on mechanism and controlling strategy of orthotropic slab buckling rockburst. *Chin J Geotech Eng* 39:1–10 (in Chinese)
- Gong Q, Yin L, Wu S, Zhao J, Ting Y (2012) Rockburst and slabbing failure and its influence on TBM excavation at headrace tunnels in Jinping II hydropower station. *Eng Geol* 124:98–108
- Gonnerman HF (1925) Effect of size and shape of test specimen on compressive strength of concrete. *Proc ASTM* 25:237–250
- Haimson BC, Chang C (2000) A new true triaxial cell for testing mechanical properties of rock, and its use to determine rock strength and deformability of Westerly granite. *Int J Rock Mech Min Sci* 37:285–296
- Haimson BC, Chang C (2002) True triaxial strength of the KTB amphibolite under borehole wall conditions and its use to estimate the maximum horizontal in situ stress. *J Geophys Res Solid Earth* 107:2257
- He MC, Miao JL, Li DJ, Wang CG (2007) Experimental study on rockburst processes of granite specimen at great depth. *Chin J Rock Mech Eng* 26:865–876 (in Chinese)
- He MC, Miao JL, Feng JL (2010) Rockburst process of limestone and its acoustic emission characteristics under true-triaxial unloading conditions. *Int J Rock Mech Min Sci* 47:286–298
- Hudson JA, Crouch SL, Fairhurst C (1972) Soft, stiff and servo-controlled testing machines: a review with reference to rock failure. *Eng Geol* 6:155–189
- Ingraham MD, Issen KA, Holcomb DJ (2013) Response of Castlegate sandstone to true triaxial states of stress. *J Geophys Res Solid Earth* 118:536–552. <https://doi.org/10.1002/jgrb.50084>
- Jimenez R, Ma XD (2013) A note on the strength symmetry imposed by Mogi's true-triaxial criterion. *Int J Rock Mech Min Sci* 64:17–21
- Johnson JW (1943) Effect of height of test specimens on compressive strength of concrete. *ASTM Bull* 23:19–21
- Kaiser PK, Cai M (2012) Design for rock support system under rockburst condition. *J Rock Mech Geotech Eng* 4:215–227
- Lee H, Haimson BC (2011) True triaxial strength, deformability, and brittle failure of granodiorite from the San Andreas fault observatory at depth. *Int J Rock Mech Min Sci* 48:1199–1207
- Li DY, Li CC, Li XB (2011) Influence of sample height-to-width ratios on failure mode for rectangular prism samples of hard rock loaded in uniaxial compression. *Rock Mech Rock Eng* 44:253–267
- Li XB, Yao JR, Du K (2013) Preliminary study for induced fracture and non-explosive continuous mining in high-geostress hard rock mine—a case study of Kaiyang phosphate mine. *Chin J Rock Mech Eng* 32:1101–1111 (in Chinese)
- Li XB, Du K, Li DY (2015) True triaxial strength and failure modes of cubic rock specimens with unloading the minor principal stress. *Rock Mech Rock Eng* 48:2185–2196
- Lin H, Cao P, Wang YX (2013) Numerical simulation of a layered rock under triaxial compression. *Int J Rock Mech Min Sci* 60(6):12–18
- Ma XD, Haimson BC (2016) Failure characteristics of two porous sandstones subjected to true triaxial stresses. *J Geophys Res Solid Earth* 121:6477–6498. <https://doi.org/10.1002/2016JB012979>
- Manouchehrian A, Cai M (2015) Simulation of unstable rock failure under unloading conditions. *Can Geotech J* 53:1–13
- Martin CD, Maybee WG (2000) The strength of hard-rock pillars. *Int J Rock Mech Min Sci* 37:1239–1246
- Michelis P (1985) A true-triaxial cell for low and high pressure experiments. *Can Geotech J Geomech Abstr* 22:183–188
- Mogi K (1966) Some precise measurements of fracture strength of rocks under uniform compressive stress. *Rock Mech Eng Geol* 4:41–55
- Mogi K (1970) Effect of the triaxial stress system on rock failure. *Rock Mech Japan* 1:53–55
- Mogi K (1971a) Fracture and flow of rocks under high triaxial compression. *J Geophys Res* 76:1255–1269. <https://doi.org/10.1029/JB076i005p01255>
- Mogi K (1971b) Effect of the triaxial stress system on the failure of dolomite and limestone. *Tectonophysics* 11:111–127
- Mogi K (1972) Effect of the triaxial stress system on fracture and flow of rocks. *Phys Earth Planet Inter* 5:318–324
- Mogi K (2007) *Experimental rock mechanics*. CRC Press, London
- Murrell SAF (1965) The effect of triaxial stress systems on the strength of rocks at atmospheric temperatures. *Geophys J Int* 10:231–281
- Nadai A, Hodge PG (1950) *Theory of flow and fracture of solids*, vol 1. McGraw-Hill, New York
- Obert L, Windes SL, Duvall WI (1946) Standardized tests for determining the physical properties of mine rock. *U S Bur Mines Rep Invest* 3891:1
- Ortlepp WD (1997) Rock fracture and rockbursts: an illustrative study. South African Institute of Mining and Metallurgy, Johannesburg
- Ortlepp WD, Stacey TR (1994) Rockburst mechanisms in tunnels and shafts. *Tunn Undergr Space Technol* 9:59–65
- Pechmann JC, Walter WR, Nava SJ, Arabasz WJ (1995) The February 3, 1995, ML 5.1 seismic event in the Trona mining district of southwestern Wyoming. *Seismol Res Lett* 66:25–34
- Sahouryeh E, Dyskin AV, Germanovich LN (2002) Crack growth under biaxial compression. *Eng Fract Mech* 69:2187–2198
- Sakurai S, Serata S (1967) Mechanical properties of rock salt under three dimensional loading conditions. In: 10th Japan Congress on testing materials, vol 10, pp 139–142
- Sriapai T, Walsri C, Fuenkajorn K (2013) True-triaxial compressive strength of Maha Sarakham salt. *Int J Rock Mech Min Sci* 61:256–265
- Takahashi M, Koide H (1989) Effect of the intermediate principal stress on strength and deformation behavior of sedimentary rocks at the depth shallower than 2000 m. In: Maury V, Fourmaintraux D (eds) *Rock at great depth*, vol 1. Balkema, Rotterdam, pp 19–26
- Vernik L, Zoback MD (1992) Estimation of maximum horizontal principal stress magnitude from stress—induced well bore breakouts in the Cajon Pass scientific research borehole. *J Geophys Res Solid Earth* 97:5109–5119. <https://doi.org/10.1029/91JB01673>
- Wawersik W, Carlson L, Holcomb D, Williams R (1997) New method for true-triaxial rock testing. *Int J Rock Mech Min Sci* 34:330
- Wen ZJ, Wang X, Tan YL, Zhang HL, Huang WP, Li QH (2016) A study of rockburst hazard evaluation method in coal mine. *Shock Vib* 16:1–9



- Wiebols GA, Cook NGW (1968) An energy criterion for the strength of rock in polyaxial compression. *Int J Rock Mech Min Sci Geomech Abstr* 5:529–549
- Xie HP, Peng RD, Ju Y, Zhou HW (2005) On energy analysis of rock failure. *Chin J Rock Mech Eng* 24:2603–2608 (in Chinese)
- You MQ (2009) True-triaxial strength criteria for rock. *Int J Rock Mech Min Sci* 46:115–127
- Zhang CQ, Feng XT, Zhou H, Qiu S, Wu W (2015) Case histories of four extremely intense rockbursts in deep tunnels. *Rock Mech Rock Eng* 45:275–288
- Zhao XG, Cai M (2014) Influence of specimen height-to-width ratio on the strainburst characteristics of Tianhu granite under true-triaxial unloading conditions. *Can Geotech J* 52:890–902
- Zhao F, He MC (2016) Size effects on granite behavior under unloading rockburst test. *Bull Eng Geol Environ* 76(3):1183–1197
- Zhao XG, Wang J, Cai M, Cheng C, Ma LK, Su R, Zhao F, Li DJ (2014) Influence of unloading rate on the strainburst characteristics of Beishan granite under true-triaxial unloading conditions. *Rock Mech Rock Eng* 47:467–483
- Zhu WC, Yang WM, Li XJ, Xiang L, Yu DJ (2014) Study on splitting failure in rock masses by simulation test, site monitoring and energy model. *Tunn Undergr Sp Technol* 41:152–164